

A catalogue of cataclysmic variables from 20 years of the Sloan Digital Sky Survey with new classifications, periods, trends and oddities.

Keith Inight,¹★ Boris T. Gänsicke,¹ Elmé Breedt,² Henry T. Israel,⁶ Stuart P. Littlefair,⁶ Christopher J. Manser,^{1,4} Tom R. Marsh,¹ Tim Mulvany,¹ Anna Francesca Pala,³ John R. Thorstensen⁵

¹*Department of Physics, University of Warwick, Coventry, CV4 7AL, UK*

²*Institute of Astronomy, University of Cambridge, Madingley Road, Cambridge CB3 0HA, United Kingdom*

³*European Space Agency, European Space Astronomy Centre, Camino Bajo del Castillo s/n, Villanueva de la Cañada, E-28692 Madrid, Spain*

⁴*Astrophysics Group, Department of Physics, Imperial College London, Prince Consort Rd, London, SW7 2AZ, UK*

⁵*Department of Physics and Astronomy, Dartmouth College, Hanover NH 03755, USA*

⁶*Department of Physics and Astronomy, University of Sheffield, Sheffield S3 7RH, UK*

Accepted XXX. Received YYY; in original form ZZZ

ABSTRACT

We present a catalogue of 507 cataclysmic variables (CVs) observed in SDSS I to IV including 70 new classifications collated from multiple archival data sets. This represents the largest sample of CVs with high-quality and homogeneous optical spectroscopy. We have used this sample to derive unbiased space densities and period distributions for the major sub-types of CVs. We also report on some peculiar CVs, period bouncers and also CVs exhibiting large changes in accretion rates. We report 70 new CVs, 59 new periods, 178 unpublished spectra and 262 new or updated classifications. From the SDSS spectroscopy, we also identified 18 systems incorrectly identified as CVs in the literature. We discuss the observed properties of 13 peculiar CVs, and we identify a small set of eight CVs that defy the standard classification scheme. We use this sample to investigate the distribution of different CV sub-types, and we estimate their individual space densities, as well as that of the entire CV population. The SDSS I to IV sample includes 14 period bounce CVs or candidates. We discuss the variability of CVs across the Hertzsprung-Russell diagram, highlighting selection biases of variability-based CV detection. Finally, we searched for, and found eight tertiary companions to the SDSS CVs. We anticipate that this catalogue and the extensive material included in the Supplementary Data will be useful for a range of observational population studies of CVs.

Key words: white dwarfs, dwarf novae, cataclysmic variables

1 INTRODUCTION

Cataclysmic variables (CVs, see Warner 1995 for an exhaustive overview) are an important class of white dwarf binaries within multiple astrophysical contexts, including accretion disc physics (González Martínez-País et al. 2014) and potential gravitational wave sources for LISA (Danzmann & LISA Study 1996). These compact binaries will become increasingly important as the inventory becomes more complete and the emerging population statistics can be used to test evolutionary models. Although $\sim 10\,000$ CV candidates are known (see for example Watson et al. 2017) that sample contains a fair amount of contaminants, including flaring M-dwarfs, young stellar objects, variable AGN and unexplained transients (see

discussion in section 2 of Pala et al. 2020). To be useful for evolutionary modelling a sample of CVs needs not only to be reasonably complete over a given volume but also possess astrometric data for each CV and, crucially, an identification spectrum.

The sample of 507 CVs spectroscopically observed by the Sloan Digital Sky Survey (SDSS) (Gunn et al. 1998; York et al. 2000) presented here is a magnitude-limited sample covering over 25.6 per cent of the sky (section 6.4.4).

The four phases of SDSS (hereafter SDSS I to IV) were executed between 2000 and 2020 (Abazajian et al. 2003; Adelman-McCarthy et al. 2008; Aihara et al. 2011; Aguado et al. 2019) and addressed many science goals of which the search for quasars (Richards et al. 2002) and latterly luminous red galaxies and quasars (Dawson et al. 2013) in the Baryon Oscillation Spectroscopic Survey (BOSS and eBOSS) are of particular relevance here. Between

★ E-mail: keith.inight@gmail.com

2000 and 2009 SDSS obtained photometry, using the five *ugriz* filter passbands, of over 14 000 square degrees, predominantly of the northern sky. The imaging camera (Gunn et al. 1998) was installed on a purpose-built 2.5 m telescope at Apache Point, New Mexico. This photometry was used to select targets for subsequent spectroscopic surveys using a multi-object, fibre-fed spectrograph capable of taking 640 (SDSS I and II) and 1000 (SDSS III and IV) simultaneous spectra spanning $\approx 3800 - 9200 \text{ \AA}$ (SDSS I and II) and $\approx 3600 - 10000 \text{ \AA}$ (SDSS III and IV, Smee et al. 2013).

Whereas CVs were targeted within SDSS I via a multi-dimensional colour selection (Szkody et al. 2002), the vast majority of CVs were serendipitously identified from the spectroscopy of quasar candidates. SDSS I (York et al. 2000) and II (Dilday et al. 2005; Yanny et al. 2009) have proven to be a major source of optical spectroscopy of CVs, both of previously known systems and new discoveries (Szkody et al. 2002, 2003, 2004, 2005, 2006, 2007, 2009, 2011).

SDSS III and IV were two subsequent phases spanning from July 2008 until June 2014 (Eisenstein et al. 2011; Dawson et al. 2013) and from July 2014 until August 2020 (Blanton et al. 2017; Dawson et al. 2016) respectively.

SDSS I and II yielded spectra of 285 CVs (Szkody et al. 2011) and have been particularly successful in identifying CVs with no history of outbursts (Gänsicke et al. 2009). Specifically they provided a rich source of short period (80 – 86 min) CVs that provided the crucial observational evidence for the existence of a “period minimum spike”. Other groundbreaking achievements include the identification of low accretion rate, X-ray weak, polars (Schmidt et al. 2008 and references therein) and CVs with pulsating white dwarfs (Woudt et al. 2005; Gänsicke et al. 2006; Mukadam et al. 2007). Beyond these individual discoveries the systematic detection of all types of CVs has enabled statistical studies of population density and CV evolution (Gänsicke 2005). These achievements from SDSS I and II provided the motivation to identify CVs in SDSS III and IV. Further motivation came from the opportunity to refine the attributes of the known CVs using new astrometric and photometric survey data.

We report here the identification of 70 new CVs found in SDSS I to IV (see list in Appendix A). We have also revisited the remaining 437 CVs observed during SDSS I to IV in the light of *Gaia* (Gaia Collaboration 2020) astronomy and photometry from the Catalina Real-Time Transient Survey (CRTS, Djorgovski et al. 2011), Zwicky Transient Facility (ZTF, Masci et al. 2018; Bellm et al. 2019) and the Transiting Exoplanet Survey Satellite (*TESS*, Ricker et al. 2015) which was not previously available. This has resulted in 59 new orbital periods (including some unpublished orbital periods from other sources, details are provided in the supplementary data) and 262 new/revised classifications. SDSS objects are identified by their coordinates, e.g. SDSS J152212.20+080340.9, which we abbreviate throughout the paper as J1522+0803.

The paper is laid out as follows. We discuss CV evolution in section 2 and in section 3 we provide an overview describing how the different types evolve in the overall CV life-cycle using examples from SDSS I to IV. In section 4 we describe the methods used to identify new CVs and classify existing ones. Our results are described in section 5 and discussed in section 6 with an overall summary in section 7.

2 CV EVOLUTION

Whilst we do not seek to replicate the extensive literature on CVs (a comprehensive coverage can be found in Warner 1995 and Hellier 2001) we do explain the evolutionary relevance of the different types of CV found by SDSS.

CVs are born out of a common-envelope event (Paczynski 1976; Ivanova et al. 2013) in which the higher-mass star in a binary system evolves off the main sequence and becomes a giant, engulfing its lower-mass companion. Friction in the common envelope extracts angular momentum and energy, resulting in a dramatic reduction in the orbital separation of the two stars. The result of the common envelope is a close binary consisting of a white dwarf (the core of the former red giant) plus a low-mass companion; this is known as a post common envelope binary (PCEB). Most PCEBs exit the common envelope in a detached configuration (and many are observed in this state, e.g. Rebassa-Mansergas et al. 2012). However, the stellar wind from the companion causes magnetic braking (Verbunt & Zwaan 1981) and results in a loss of angular momentum. Meanwhile tidal forces on the secondary will eventually result in tidal locking to the orbital period (Fleming et al. 2019). Magnetic braking will eventually shrink the orbital separation to the point where the secondary star fills its Roche lobe, and starts mass transfer onto the white dwarf – initiating the further evolution of the system as a CV.

Magnetic braking continues into the CV phase resulting in the system continuing to lose angular momentum and as a consequence the system separation and P_{orb} will decrease.

At around $P_{\text{orb}} = 3\text{h}$ the donor stars in CVs become fully convective, possibly resulting in a re-configuration of their magnetic field (see observational evidence in Reiners & Basri 2009 and also fig. 15 in Kochukhov 2021). In the standard scenario of CV evolution (Knigge et al. 2011), magnetic braking is strongly reduced, and the donor star, slightly bloated due to prior mass loss, shrinks to its thermal equilibrium radius, detaching from the Roche-lobe and stopping the mass transfer. The observational motivation for this “disrupted magnetic braking scenario” (Rappaport et al. 1983) is a paucity of CVs within the range $2.15\text{h} \lesssim P_{\text{orb}} \lesssim 3.18\text{h}$; this is the so-called “period gap” (Whyte & Eggleton 1980; Howell et al. 2001; Knigge 2006). Some of this under-representation appears to be due to selection effects (see for example fig. 9 in Inight et al. 2021 and section 6.1). In the case of strongly magnetic white dwarfs, magnetic braking could be reduced, and these systems may not experience a detached phase in their evolution (Webbink & Wickramasinghe 2002).

For periods $\lesssim 3\text{h}$, gravitational radiation (Paczynski 1967; King 1988) supersedes magnetic braking as the primary cause of angular momentum loss, which will eventually cause the separation and orbital period to decrease sufficiently for the donor to fill its Roche lobe and the system to resume accretion as a CV.

Throughout the evolution of a CV the mass of the donor, the rate of mass loss from the donor (\dot{M}), and P_{orb} all continue to decrease until the donor mass is too low to sustain hydrogen burning and the system becomes a brown dwarf. This point is the “period minimum” of the system (Paczynski & Sienkiewicz 1983). Following further mass loss from the donor the orbital separation (and hence period) increases and it becomes a “period bouncer” (e.g. Pala et al. (2018)).

The previous discussion has assumed that the donor is still on the main sequence when it commences accretion. However the donors in some CVs have undergone substantial nuclear evolution. Because the orbital period at which a donor fills its Roche lobe

is related to its density ρ_d via $P_{\text{orb}} \propto (\rho_d)^{-0.5}$ (equation 12 in Knigge et al. 2011) it follows that, for the same donor mass, CVs with nuclear evolved donors have longer orbital periods than their un-evolved counterparts (e.g. Rodríguez-Gil et al. 2009). At periods $\lesssim 5$ h, evolved donors have a higher temperature and spectral type than main sequence stars of the same mass. They can appear in the period gap (Rebassa-Mansergas et al. 2014) and evolve to periods below the period minimum (Thorstensen et al. 2002b).

3 CV SUB-TYPES

“Cataclysmic Variables” were named as such because of the large brightness variations (eruptions and outbursts) observed among classical novae and dwarf novae. The modern definition of a CV dates from the 1960’s (see for example Kraft 1963) and consists of a semi-detached binary in which a white dwarf accretes from a Roche-lobe filling donor star – and the current roster of CVs includes many systems that have no recorded outbursts (Gännsicke et al. 2009).

CVs are classified into a number of sub-types. Historically they have been categorised based upon their observable characteristics with categories typically being named after a prototype system, frequently the first discovery. The number of sub-types, their definition, and relationship between different sub-types remain in flux, making their use challenging for scientists not regularly working in this research area – and some care has to be taken with the temptation to define new sub-types for each additional observational wrinkle in a particular CV. Nevertheless, dividing CVs into sub-types is meaningful, as their observational characteristics depend on a small number of physical parameters, which link to the evolutionary state and the accretion geometry of an individual system (see Fig. 1).

Here we provide an overview of the main CV categories that have been historically used with examples from SDSS I to IV and detail their state of evolution and mode of accretion. The key physical parameters are the orbital period, P_{orb} , the rate of mass loss from the donor, \dot{M} , and the white dwarf magnetic field strength, B .

The strength of the magnetic field of the white dwarf is of particular importance in determining the accretion geometry (Norton et al. 2008). We therefore discuss the classification and evolution of magnetic and non-magnetic systems separately.

3.1 Non-magnetic CVs

3.1.1 Dwarf Novae

The dwarf nova thermal limit cycle starts with increasing mass being retained in the disc which continues to grow until it becomes thermally unstable and a dwarf nova occurs. The magnitude of a dwarf nova outburst is typically $\Delta m = 3 - 5$ (Meyer & Meyer-Hofmeister 1983) and typically lasts for a few days (although superoutbursts such as that of GW Lib in 2007 can reach $\Delta m \approx 9$ and last several weeks) after which the disc cools and the cycle repeats itself. Four sub-types are discussed below (SU UMa, WZ Sge, ER UMa and Z Cam) with the remaining dwarf nova CVs being classified as U Gem. In quiescence dwarf nova spectra (Fig. 2) exhibit hydrogen and also sometimes helium emission lines whilst in outburst their spectra resemble those of novalike variables (see below).

3.1.1.1 SU UMa dwarf novae are characterised by occasional “superoutbursts” (Fig. 3) typically lasting several weeks and recurring with a supercycle of a few hundred days (Osaki 1989; Buat-

Ménard & Hameury 2002; Patterson et al. 2005b). These superoutbursts are significantly brighter than the regular dwarf novae which occur in between the superoutbursts. Hirose & Osaki (1990) showed that as the separation of CVs decreases tidal forces eventually cause the disc to become eccentric and non-axisymmetric. The material in the outer edge of the disc rotates more rapidly than the orbital period and will stabilise at a resonant ratio of 3:1. The gradual accumulation of mass in the disc eventually results in a superoutburst; Hirose & Osaki (1990) showed analytically that superoutbursts only occur when $q = M_d/M_{\text{WD}} \lesssim 0.3$, with M_{WD} and M_d the masses of the white dwarf and of the donor star. Assuming a typical value of $M_{\text{WD}} \approx 0.8 M_{\odot}$ and using the relation $M_d \approx 0.065 P_{\text{orb}}^{5/4}$ (Warner 1995 section 2.8) implies $P_{\text{orb}} \lesssim 2.8$ h. After reaching the peak luminosity, the superoutburst light curves are modulated by periodic oscillations called superhumps. The superhump period is a few per cent longer than P_{orb} and the relation $P_{\text{orb}} = 0.9162 \times P_{\text{sh}} + 5.39/60$ h can be used to estimate P_{orb} (Gännsicke et al. 2009). In reverse, if P_{sh} and P_{orb} are both measured, the superhump period excess $\epsilon = (P_{\text{sh}} - P_{\text{orb}})/P_{\text{orb}}$ can be used to estimate q (Patterson et al. 2005b; Kato & Osaki 2013) (note that the latter authors distinguish between the slightly different superhump periods observed as the superoutbursts evolve).

3.1.1.2 ER UMa Dwarf novae (Fig. 4) are a sub-type of SU UMa CVs characterised by an unusually short supercycle (20 – 50 d) so that they spend over a third of the time in superoutburst. The intervening time between superoutbursts is punctuated by normal outbursts every few days (Robertson et al. 1995; Kato et al. 2013). The cause for this behaviour is an \dot{M} around four times that of a typical SU UMa CV.

3.1.1.3 WZ Sge dwarf novae are also a sub-type (Patterson et al. 2002; Kato 2015) of SU UMa CVs. Their donors have lost most of their mass and they have low \dot{M} with very infrequent, albeit bright, superoutbursts (Fig. 5). Most WZ Sge systems do not exhibit normal outbursts in between their superoutbursts. The low \dot{M} and consequential low disc luminosity, often result in the white dwarf being visible in the optical spectrum. In many cases this is the best evidence for a WZ Sge classification as commonly used definitions (Kato et al. 2001; Kato 2015) are based upon observation of an outburst, together with the characteristic early superhumps, which may not occur for decades. Note that low \dot{M} is not sufficient in itself for a classification; there also needs to be evidence of the low mass of the donor.

3.1.1.4 Z Cam dwarf novae are dwarf novae with the unusual characteristic (Fig. 6) of having “standstills” of luminosity midway between the quiescent level and the elevated level associated with a dwarf nova outburst (Simonsen et al. 2014). This is believed to be due to having an \dot{M} that fluctuates around the critical level and is too high to sustain the thermal limit cycle associated with dwarf novae. The IW And stars (Hameury & Lasota 2014) form a sub-category of Z Cam and show continual outbursts (not unlike dwarf novae) during the “standstill”.

3.1.2 Classical Novae

Classical novae (Bode & Evans 2012) were first observed by ancient Chinese astronomers as eruptions with $\Delta m = 8 - 15$ that decayed over a period of a few to several hundred days (Clark et al. 1977). They are caused by an accumulation of hydrogen on the surface

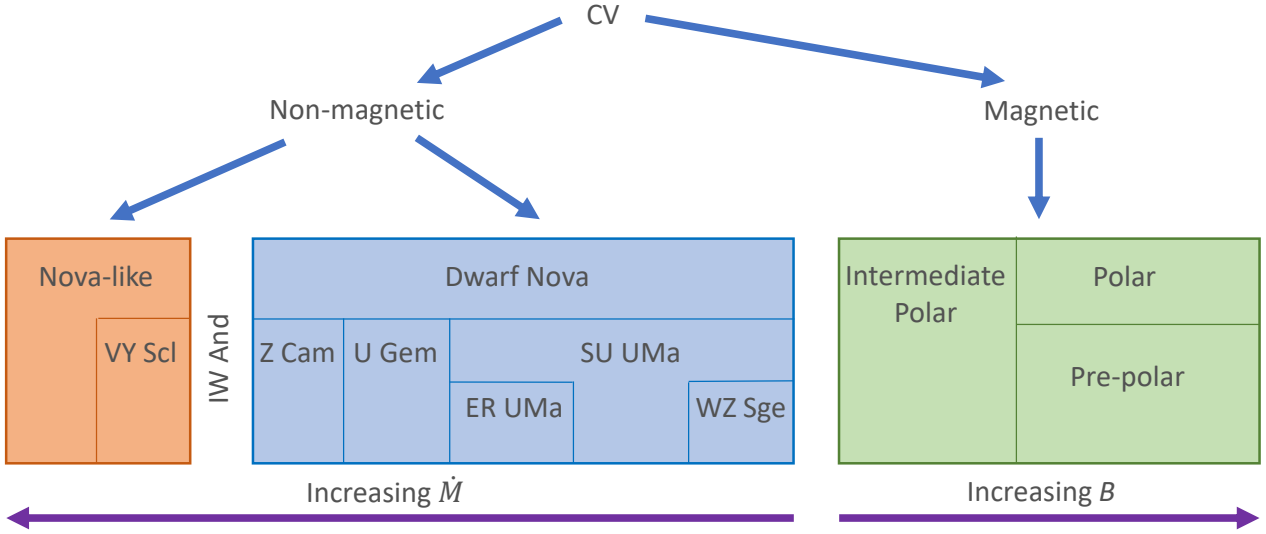


Figure 1. Diagram depicting the CV classification scheme used in this paper. The physical key parameters that define the boundaries between different classes are \dot{M} and P_{orb} (which, together, establish whether or not the accretion disc is subject to thermal instabilities) and B (which determines whether or not a disc forms in the first place). Depending on the exact physical setup, some individual CVs may straddle the boundaries between the sub-types defined above. AM CVn systems, with three possible formation channels (Section 3.1.4), follow the same distribution as non-magnetic CVs.

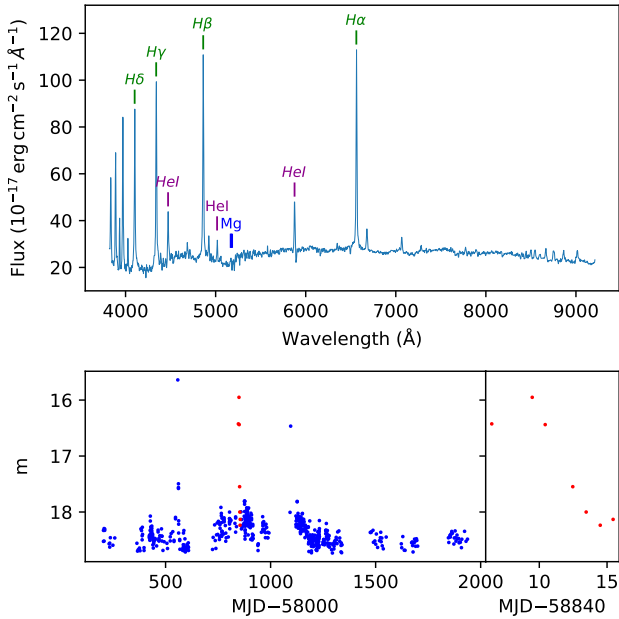


Figure 2. J0813+4528 is an example of a dwarf nova. Top panel: The quiescent SDSS spectrum (smoothed with a five-point box-car filter) shows strong emission lines. The continuum reveals the spectroscopic signatures of the donor star, indicative of a long orbital period (6.94 h); this is a U Gem type dwarf nova above the period gap. Bottom left panel: ZTF (*g*-band) light curve showing outbursts. Bottom right panel: Expanded light curve of the outburst highlighted in red in the bottom left panel showing the decay over ≈ 3 d.

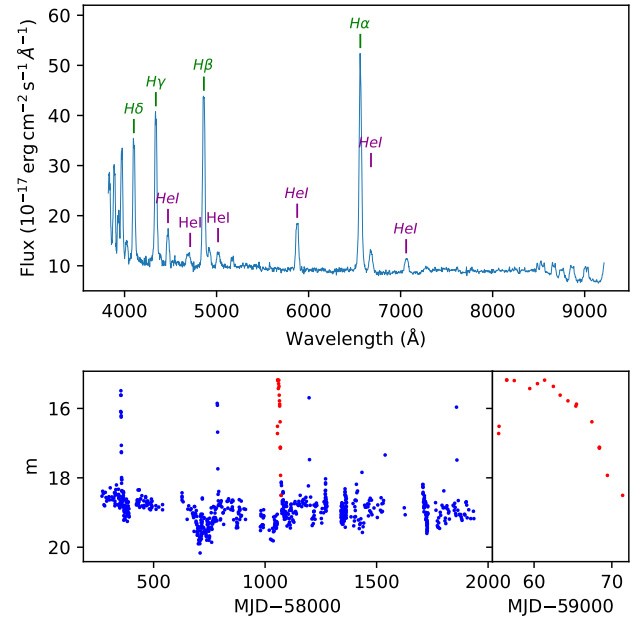


Figure 3. J0032+3145 is an example of an SU UMa CV. Top panel: Smoothed SDSS spectrum in quiescence showing the typical, slightly double-peaked, Balmer emission lines. The Helium emission lines are not always present in SU UMas. Bottom left panel: ZTF (*g*-band) light curve showing outbursts and a superoutburst in red. Bottom right panel: Expanded light curve showing the decay of the superoutburst and characteristic superhumps.

of the white dwarf which eventually reaches a critical mass and pressure thereby initiating a runaway nuclear reaction (Starrfield 1971) that expels an expanding shell (Cohen & Rosenthal 1983; Shara et al. 2012) and may also influence the evolution of the CV

(Nelemans et al. 2016; Shen & Quataert 2022) by causing frictional angular momentum loss (Schreiber et al. 2016). Classical novae can therefore occur in all types of CVs including magnetic ones (Stockman et al. 1988). The accumulation of hydrogen is influenced

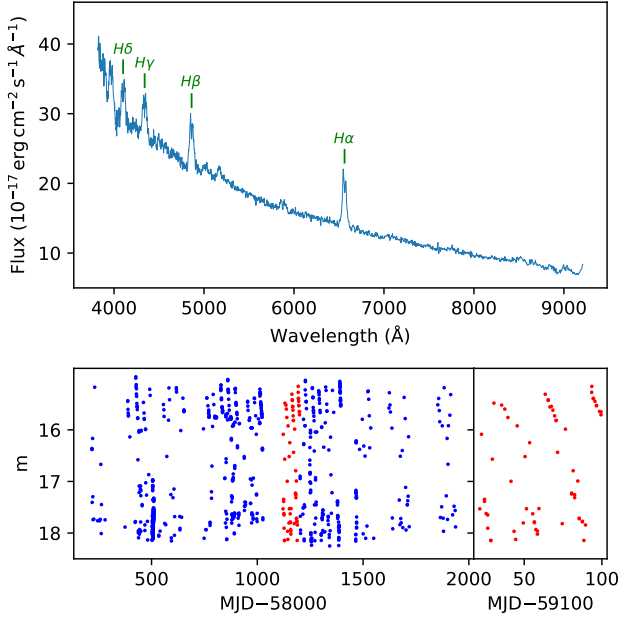


Figure 4. J0912+5053 (DIUMA) is an example of an ER UMa CV. It has a high \dot{M} which is inconsistent with its short orbital period of 78 min at the period minimum (Kato et al. 1996; Fried et al. 1999), resulting in extremely frequent superoutbursts. The supercycle is 25 d whilst normal outbursts occur every four days. Top panel: Smoothed SDSS spectrum in quiescence showing Balmer emission lines. Bottom left panel: ZTF (g -band) light curve showing frequent superoutbursts. Bottom right panel: Expanded light curve showing the frequency of the superoutbursts.

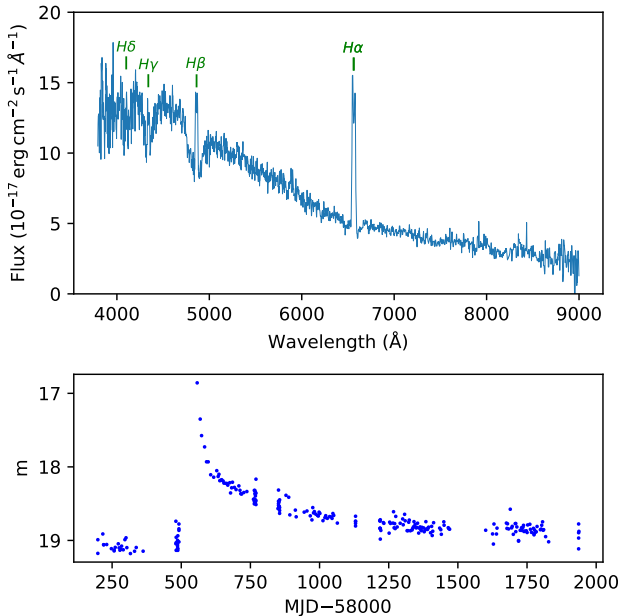


Figure 5. J1610-0102 (V386 Ser) is an example of a WZ Sge CV. Top panel: Smoothed SDSS spectrum in quiescence showing double-peaked Balmer emission lines from the accretion disc. The spectrum of the white dwarf is visible at the blue end with characteristic wide Balmer absorption lines. Bottom panel: ZTF (g -band) light curve showing a single characteristically large superoutburst. Many systems believed to be WZ Sge stars, based on their spectra and periods, have no such recorded outbursts and identification rests on other evidence such as spectra.

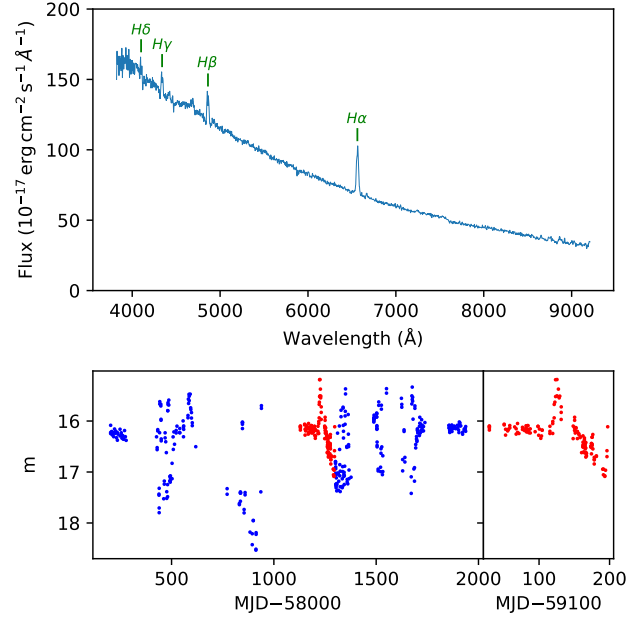


Figure 6. J1028+2148 (MV Leo) is an example of a Z Cam CV. Top panel: Smoothed SDSS spectrum in “standstill” showing Balmer emission lines. Bottom left panel: ZTF (merged and scaled r - and g -bands shown in blue) light curve showing standstill periods as well as outbursts and the low, quiescent, level. The outburst is highlighted in red. Bottom right panel: Expanded light curve showing a period of “standstill” followed by an outburst and a decline to quiescence.

by \dot{M} and therefore classical novae are more common in high \dot{M} systems typically with periods $P_{\text{orb}} \geq 3$ h.

By definition an eruption of a classical nova has been recorded at some time. The spectrum of a classical nova varies considerably depending upon the time since this eruption. The rapidly expanding shell will initially dominate the spectrum, with broad emission lines of hydrogen and helium. As it expands further and becomes more diffuse it resembles a planetary nebula and exhibits forbidden lines such as [S II] 6717 Å. The rapid expansion of the shell also results in spectral lines exhibiting P Cygni profiles. Eventually (years to decades) the spectrum becomes that of the pre-eruption CV. Most classical novae revert to being novalike variables (Fig. 7), which is unsurprising as the nova recurrence time is inversely related to the accretion rate, and hence the nova population is dominated by novalike variables (Townsend & Bildsten 2005).

3.1.3 Novalike variables

Novalike variables (Dhillon 1996) have bright spectra dominated by the hot and stable disc (Fig. 8). The hydrogen in their discs is almost fully ionised and their spectra therefore exhibit absorption lines, often with inset emission lines. They often have strong disc winds which can appear as P Cygni spectral lines (Inight et al. 2022). Novalikes sometimes exhibit changes between high and low states and observational phenomena in their light curves have given rise to a number of sub-types. The VY Scl sub-type shows relatively deep ($\Delta m = 2 - 5$) low states which can last a few weeks to about a year, during which short brightenings occur (Bruch 2019), the nature of which is still discussed (Scaringi et al. 2017). This contrasts with the IW And class (Section 3.1.1.4) in which characteristic outbursts occur during the (higher state) standstills (Kato 2019).

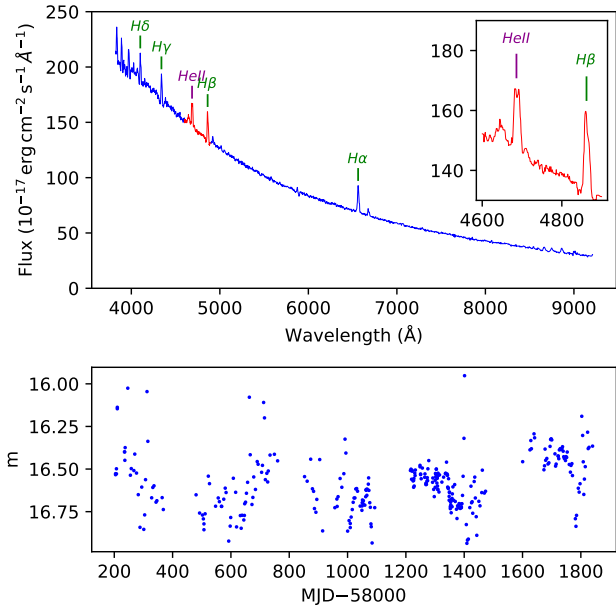


Figure 7. J1545+1422 (CT Ser) is an example of an old nova that erupted in 1948, and that now appears as a novalike variable. Top panel: Smoothed SDSS spectrum showing Balmer and He II emission lines. Top inset panel: Expanded spectrum showing the relative strength of the H β and He II lines. (Munari et al. 2014) Bottom panel: ZTF (g -band) light curve illustrating the relatively constant emission from the disc in its high state.

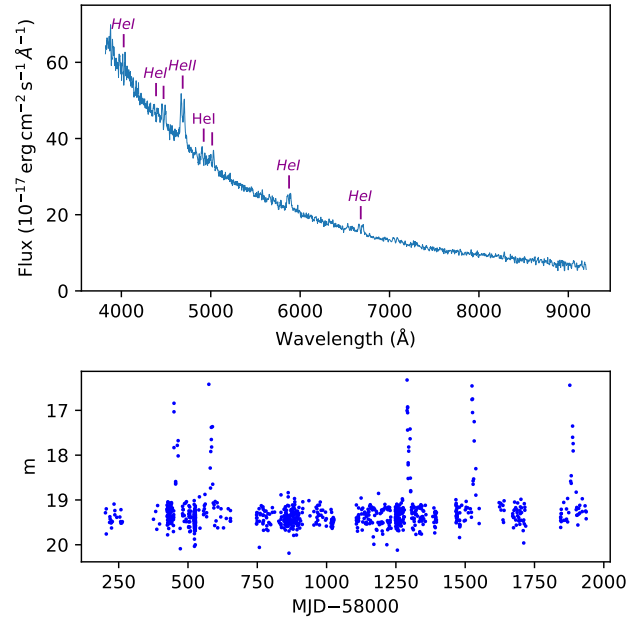


Figure 9. J0926+3624 is an example of an AMCVn CV. Top panel: The smoothed SDSS spectrum shows He I and He II emission lines but no hydrogen lines. The absence of hydrogen lines is a characteristic of AMCVn CVs. Bottom panel: ZTF (merged and scale r - and g -bands) light curve showing outbursts.

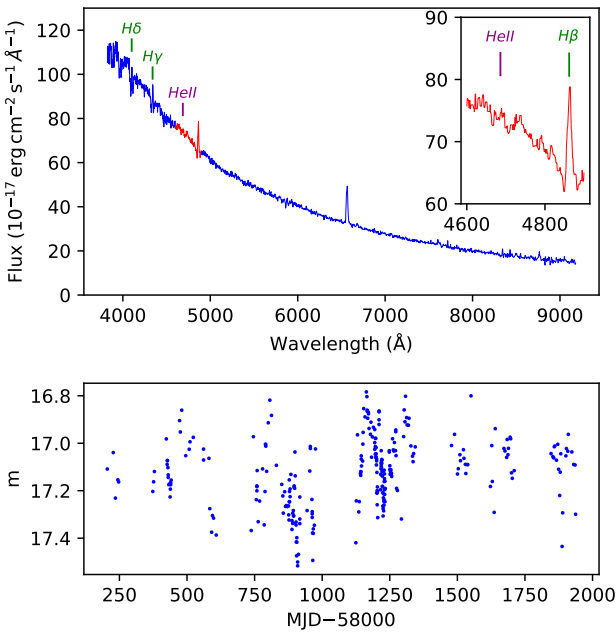


Figure 8. J0758+1043 is an example of a novalike variable. Top panel: Smoothed SDSS spectrum showing Balmer H α and H β emission lines together with H γ and H δ absorption lines. Top inset panel: Expanded spectrum showing the H β line and absence of He II lines. The strength of He II 4686 Å emission lines varies with orbital phase far more than Balmer emission lines – and often exceeding the strength of the H β line (Hoard et al. 2014). Bottom panel: ZTF (g -band) light curve showing the relatively constant emission from the disc in its hot, steady state.

3.1.4 AMCVn

AMCVn systems (Fig. 9) are identified by helium lines and an absence of hydrogen lines in the optical spectrum (Ramsay et al. 2018). They are short-period systems ($P_{\text{orb}} \approx 5 - 68$ min) but their evolutionary origin is unclear with at least three potential formation channels leading from their progenitors (Solheim 2010). AMCVn systems are rare, with only ≈ 60 systems known (Ramsay et al. 2018). They are good verification binaries for the space-based *LISA* gravitational wave detector (Amaro-Seoane et al. 2017) given their short periods and separations (Nelemans et al. 2004; Liu et al. 2021).

3.2 Magnetic CVs

Perhaps a third (Pala et al. 2020) of CVs have a white dwarf with a magnetic field $B \gtrsim 1$ MG and these are termed magnetic. The origin of this strong field is not well understood; it may be formed during the common-envelope event or sometime later (Belloni & Schreiber 2020). Schreiber et al. (2021) propose a model whereby the magnetic CV is born without a strong field and the white dwarf is spun up by accretion. The cooling white dwarf in the CV then forms a dynamo as it crystallises. The strengthening magnetic field causes the system to become detached and the only accretion is from the donor wind which follows magnetic field lines. This pre-polar stage (Hakala et al. 2022) continues until after the donor becomes fully convective and mass transfer recommences at which point the CV is a polar or intermediate polar (Wilson et al. 2021). This model is consistent with observational evidence (fig. 9 in Ferrario et al. 2015) as intermediate polars (with $B \lesssim 10$ MG) are, in general, observed to have orbital periods $P_{\text{orb}} \gtrsim 3$ h whilst polars (with $B \gtrsim 10$ MG) are observed to have typical orbital periods $P_{\text{orb}} \lesssim 2$ h.

3.2.1 Polar

The magnetic field of the white dwarf in polars (Cropper 1990; Wu 2000), typified by the prototype AM Her, is generally greater than 10 MG. In this case the Alfvén radius is beyond the circularisation radius, preventing the formation of an accretion disc, and the accretion flow follows field lines from the inner Lagrange point to impact on the white dwarf. These shock-heated impact zones ($\approx 10^8$ K) give rise to X-ray radiation and also characteristic He II emission lines (Fig. 10). The cyclotron radiation is sometimes observed in spectra as “humps” (see for example Thomas et al. 2000). These humps are harmonics of the cyclotron frequency $f = (eB)/(2\pi m_e)$, with e and m_e the charge and the mass of the electron, due to the magnetic field B and can appear in the infrared (e.g. AM Her, $B \approx 15$ MG Bailey et al. 1991), optical (e.g. MR Ser, $B \approx 25$ MG; Schwöpe et al. 1993) or ultraviolet (e.g. AR UMa, $B \approx 200$ MG; Gänsicke et al. 2001) according to field strength. Cyclotron emission is directional and results in cyclotron beaming which manifests itself as periodic behaviour. Polars can also be identified either by polarimetry, as cyclotron radiation is polarised (Chanmugam & Dulk 1981; Shahbaz 2019), or by the Zeeman splitting of Balmer lines from the white dwarf (Ferrario et al. 1995) that is sometimes visible in spectra obtained during low states when accretion nearly ceases (Fig. 11) and can be used to estimate the strength of the magnetic field. A consequence of the strong magnetic field is that the spin period of the white dwarf normally equals P_{orb} . This is thought to be due to the interaction of the strong white dwarf magnetic field with the donor magnetic field generating a torque which over time causes the white dwarf to spin down until it equals P_{orb} ; the equilibrium situation (Campbell 1984). Asynchronous polars (Piirola et al. 1994; Campbell & Schwöpe 1999) have a white dwarf spin period slightly different from P_{orb} which can be detected in periodograms. Asynchronous polars are believed to have been knocked out of exact synchronisation by an event such as a nova (Pavlenko et al. 2018).

3.2.2 Pre-polars

White dwarfs in pre-polars (Reimers et al. 1999; Schwöpe et al. 2002a; Parsons et al. 2021) (also called low-accretion rate polars) accrete via a stellar wind from the donor rather than through Roche-lobe overflow. These detached systems therefore have very low accretion rates with \dot{M} less than one per cent of that of other CVs (Schmidt et al. 2005). Cyclotron humps are the defining characteristic of pre-polars; typically the second and third harmonics are visible in the optical – although the humps can be masked by the donor spectrum (Fig. 12). Their cyclotron emission does exhibit circular polarisation (Hakala et al. 2022), but they have very low X-ray luminosities (Vogel et al. 2011). In the evolution scenario of Schreiber et al. (2021) pre-polars represent a natural phase in the evolution of CVs once the white dwarf develops a strong magnetic field.

3.2.3 Intermediate polars

Intermediate polars (Patterson 1994) such as their prototype DQ Her, have weaker white dwarf magnetic fields than polars. The magnetic field is too weak to force synchronisation of the spin period of the white dwarf resulting in a spin period significantly shorter than the orbital period (Norton et al. 2004) – the defining characteristic of an intermediate polar (Fig. 13). The vast majority of intermediate polars have a truncated accretion disc (Hameury & Lasota 2017). In common with non-magnetic CVs material from

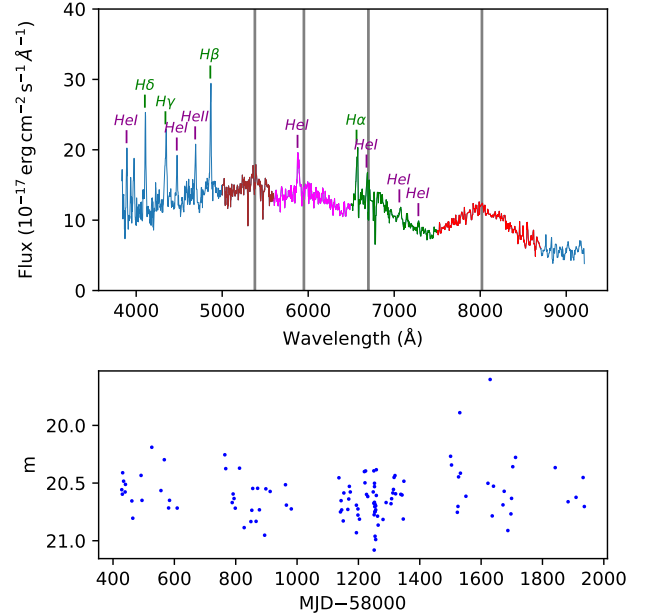


Figure 10. J0921+2038 is an example of a polar. Top panel: The smoothed SDSS spectrum (blue) shows Balmer, He I and characteristic He II emission lines. The four cyclotron humps (brown, magenta, green and red) provide clear evidence that this is a polar. Schmidt et al. (2008) determined that these are the fifth, sixth, seventh and eighth harmonics (shown in grey) due to a magnetic field of $B = 32$ MG. Bottom panel: ZTF (g -band) light curve showing the variability due to cyclotron beaming. There are no outbursts as polars do not have discs in which to store accreting material and hence they do not undergo a thermal limit cycle.

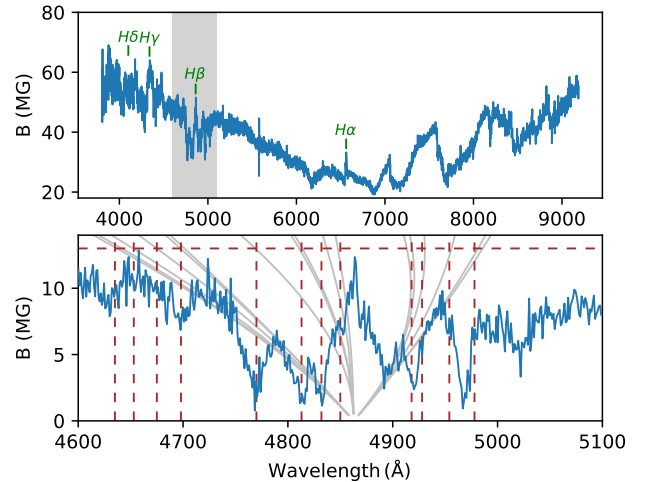


Figure 11. J1105+2506 (ST LMi) is an example of a polar showing Zeeman splitting. The spectrum is shown in the top panel. The lower panel shows a model of the $H\beta$ line evolving vertically (grey lines) with increased magnetic field (Schimeczek & Wunner 2014). The spectrum is over-plotted in blue with flux scaled to roughly match the amplitude of the grey lines. The split lines are identified by vertical dashes; they coincide with the grey lines at $B \approx 13$ MG.

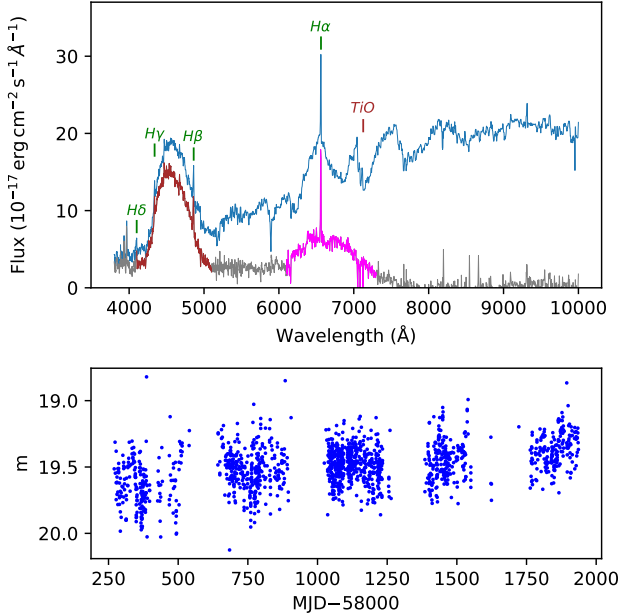


Figure 12. J0049+2226 is an example of a pre-polar. Top panel: The smoothed SDSS spectrum (blue) shows Balmer emission lines. The donor is visible at the red end of the spectrum. The cyclotron hump visible between 4200 Å and 5000 Å (brown) is clear evidence that this is a polar or pre-polar. Following Parsons et al. (2021) we subtracted a model spectrum (Kesseli et al. 2017) of an M3 dwarf (result in grey) to reveal a further cyclotron hump (magenta) at 6840 Å. Modelling of harmonic frequencies for varying magnetic fields yielded a good fit for a magnetic field strength of $B \approx 78$ MG with the humps forming the second and third harmonics. The fact that the donor is visible implies that the accretion rate is low and this implies that this is a pre-polar accreting from the donor wind (Schreiber et al. 2021). Bottom panel: ZTF (g -band) light curve showing the variability attributable to cyclotron beaming which revealed the orbital period ($P_{\text{orb}} = 5.92$ h).

the donor passes through the inner Lagrange point and pursues a ballistic path until it merges with the disc. The disc is truncated at the Alfvén radius and material then follows field lines from the innermost part of the disc to one or both magnetic poles. The presence of the disc can result in outbursts (Hameury & Lasota 2017). Magnetically funneled accretion onto the magnetic poles of the white dwarf results in pulsations in X-ray light curves (Hellier et al. 1991), which are the definitive observational proof of a CV being an intermediate polar.

4 METHODS

In compiling this CV catalogue, we followed a two-step process. In the first step we identified a shortlist of potentially new CVs from the 5 789 200 spectra of SDSS III and IV. In the second step we then undertook a detailed classification of these potential CVs, as well as revisited all the CVs previously identified in SDSS I and II.

4.1 Identification

SDSS I to IV focused upon a number of surveys none of which explicitly targeted CVs. Fortunately the (BOSS and eBOSS) (Dawson et al. 2013, 2016) targets included quasars which share a similar colour parameter space to CVs. Since the publication of the first comprehensive orbital period distribution of SDSS (Gänsicke

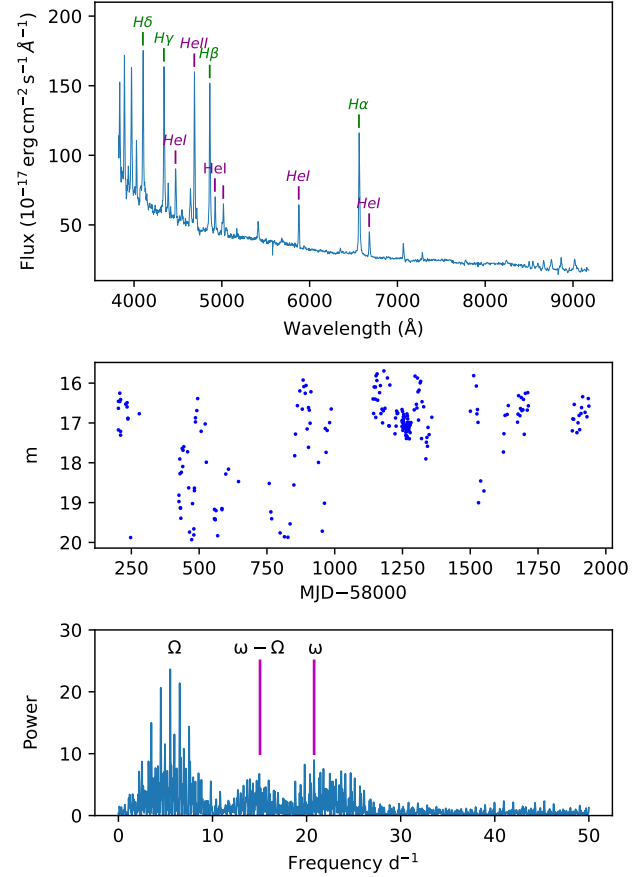


Figure 13. J0946+1350 (HY Leo, HS 0943+1404) is an example of an intermediate polar. Top panel: The smoothed SDSS spectrum shows Balmer, He I and He II emission lines. Middle panel: ZTF (g -band) light curve showing the variability due to the spin of the white dwarf and the accretion stream. The alternation between high and low states is also evident. Bottom panel: Periodogram taken from archival Jacobus Kapteyn Telescope data showing the orbital frequency (Ω), spin period (ω) and the beat period together with numerous aliases. For a detailed period analysis, see Rodríguez-Gil et al. (2005).

et al. 2009), we progressively built up a list of candidate CVs based upon visual inspection of the flux and wavelength calibrated SDSS spectra (Weaver et al. 2015; Dawson et al. 2016). The spectra were reviewed multiple times by a range of individuals using a number of pre-selections in terms of colour and filtering on the redshifts determined by the SDSS project.

This visual process was augmented by a supervised machine learning process. A data set of known CVs and proven non-CVs was used to train a Random Forest (RF) classifier (Liaw & Wiener 2001). The RF model used features extracted from the equivalent widths of 12 spectral lines and the average gradient of the spectrum measured over five intervals. The different identification methods resulted in a substantial overlap in the sub-sets of CV candidates that they identified, and whereas we cannot claim to have identified all the CVs that were spectroscopically observed by SDSS, we are confident that our search has picked up the majority of them. CVs that remain overlooked will either have extremely low signal-to-noise ratio spectroscopy, or have colours very close to those of single main-sequence stars, and weak emission lines.

4.2 Classification

No single method can reliably classify CVs – it is necessary to consider all the available information (SDSS spectroscopy, time-series photometry, *Gaia* astrometry, colours from broad-band photometry, imaging) and seek a classification of CV sub-type that is consistent with all of the data by making use of the diagnostics outlined in section 3. Where possible, we attempted to classify the SDSS CVs down to the sub-types illustrated in Fig. 1. However, in ≈ 13 per cent of cases only high level classifications such as dwarf nova or magnetic CV are possible due to the limited amount of information that is currently available. In addition, in the ≈ 20 per cent of cases where a classification is very likely but not certain a colon (:) has been appended.

We began the classification of each object with a literature search using Simbad (Wenger et al. 2000) and a search of the AAVSO VSX database (Watson et al. 2006). Where an existing classification exists we checked that it is consistent with the SDSS I to IV spectra together with data from *Gaia*, VizieR, ZTF, CRTS and *TESS*. This process resulted in refining 262 classifications. It also revealed 18 systems, previously categorised as CVs that are now known not to be CVs (see section 5.2). For each CV, the references for the initial discovery, orbital period measurement, and optical spectroscopy are documented in the Supplementary Data.

Detailed consideration of the available data is discussed in the following sections.

4.2.1 Spectral analysis

We first plotted the SDSS spectrum and then used the spectrum to calculate a synthetic *Gaia* *G*-band magnitude using the `PYTHON PYPHOT`¹ package. In addition to the SDSS spectrum we also created a broad-band (ultraviolet to infrared) spectral energy distribution (SED) diagram using data downloaded from VizieR (Allen et al. 2014) and over-plotted the spectrum. These plots are available as PNG files in the supplementary data.

We initially compared the SED with the SDSS spectrum. There can be a number of possible explanations if the spectrum is not consistent with the SED. Firstly the flux calibration of all or part of the spectrum may be faulty which we establish by comparing the synthetic magnitude with archive observations. Secondly the spectrum may have been taken at a time when the CV was in a different state to that when the photometry was obtained. Thirdly the SED may have been contaminated by flux from a nearby object – which is why we check the PanSTARRS images (see Section 4.2.4). In some cases, the photometry from VizieR traces distinct SEDs, suggesting that photometry of the system was obtained in different accretion states. In these cases, the epochs of the SED photometry can be compared with the available light curves (section 4.2.2).

We next tried to identify the donor and/or the white dwarf in the SDSS spectrum. At the blue end of the spectrum broad Balmer absorption lines are indicative of the white dwarf. Conversely if the Balmer jump is visible in emission then the disc or accretion stream is much brighter than the white dwarf, which is typical of SU UMa CVs, polars, and intermediate polars. Absorption from the Mg triplet at 5167, 5172 and 5183 Å (Fig. 2) is indicative of an early M-type or late K-type donor (suggestive of long, ≥ 2 h, orbital periods) whereas a rising continuum in the red part of the

spectrum (Fig. 5), often broken by TiO “sawtooth” molecular absorption bands indicates a mid-to-late type M dwarf (suggestive of shorter orbital periods). In addition, the detection of a blackbody-shaped bump in the ultraviolet or infrared part of the photometric SED can identify a white dwarf or M dwarf, respectively. Care was taken to distinguish the Balmer absorption lines from a white dwarf from those originating in a disc. Disc absorption lines tend to be narrower and flat-bottomed as they are formed by Doppler broadening due to Keplerian velocities in the disc whilst the Balmer absorption lines of the white dwarf are pressure-broadened due to the high surface gravities in the atmosphere. A clear white dwarf signature in the spectrum is indicative of a low level of accretion. If in addition the donor is not visible it suggests that the system is a WZ Sge candidate.

Next, we considered the emission lines detected. In addition to the Balmer and He I lines, we probed for the presence of [S II] 6717 Å which is indicative of contamination by a nebula and is not seen in CV spectra. Broad and strong emission lines at arbitrary wavelengths are associated with highly red-shifted quasars. Finally, He II 4686 Å emission is indicative of a polar or intermediate polar particularly if the ratio of its equivalent width to that of H β is greater than 0.4 (Silber 1992)

We also considered the shape of emission lines. Balmer emission lines are indicative of an accretion flow, either the disc in a non-magnetic CV, or a stream in polars. In non-magnetic CVs, the width of the Balmer emission from the disc will depend upon the inclination of the system (Horne & Marsh 1986), with broad lines and the detection of double-peaks indicating a high inclination. Furthermore deep central absorption dips embedded in broad double peaked Balmer lines are a good indication that a system is eclipsing. Asymmetric emission lines are associated with the velocity dispersion of the accretion stream of polars whilst very thin lines are typical of background nebulae and detached systems.

Lastly we also superimposed upon the SDSS spectrum the five SDSS photometric magnitudes obtained in the original observations. These can reveal inconsistencies and in particular can reveal cyclotron humps (due to one observation being taken at an orbital phase when the cyclotron emission peaked).

4.2.2 Light curves

Archival light curves from the CRTS, ZTF and *TESS* were obtained from online archives; Caltech, IRSA (Rebull et al. 2019) and Lightkurve (Lightkurve Collaboration et al. 2018) respectively. We reviewed these looking for outbursts, to provide confirmation of a dwarf nova classification, and also for eclipses to obtain orbital periods. The long span of this data (over 20 years) also reveals many state changes that are indicative of certain CVs (see Figs. 10 and 13) and novalike variables (Fig. 8). The light curves for all CVs are shown in the supplementary data. We generated periodograms in an attempt to determine orbital periods from the light curves. Prior to generating the periodogram we cropped any outbursts from the light curve which was then de-trended typically using a low-order polynomial fit. Two periodograms of the light curve were then produced using a Fourier transform and also an orthogonal multi-harmonic analysis of variance (Schwarzenberg-Czerny 1996). Potential periods were identified from peaks in the periodogram that exceeded a false alarm probability of five per cent; the results were then validated by phase-folding the original light curve on the potential period (see Fig. 14). The shape of the phase-folded light curve not only confirms that the period is valid but also helps to identify cases in which the orbital period may be twice that of the strongest signal

¹ <https://github.com/mfouesneau/pyphot>

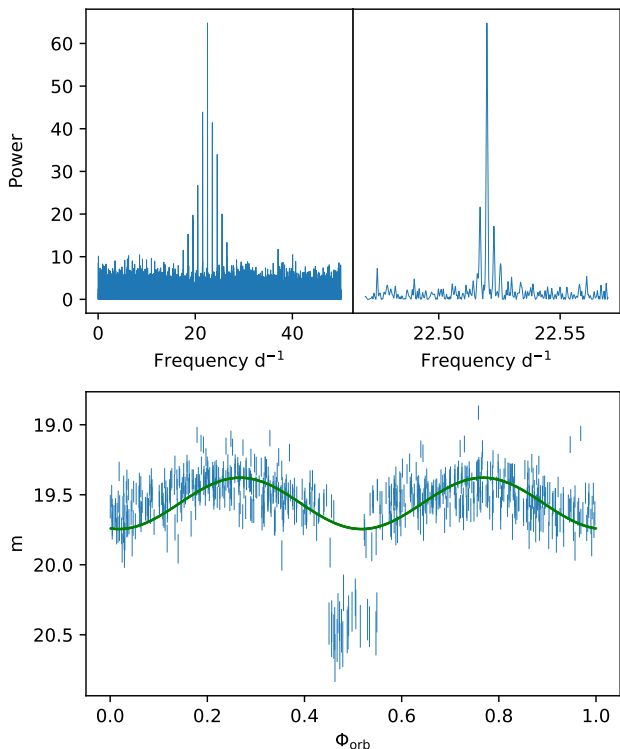


Figure 14. The Fourier transform of the ZTF light curve of J0158+2823, an eclipsing CV, yields a particularly clear periodogram. Top left panel: The aliases around the central frequency are separated by a frequency of once per day – reflecting the nightly sampling. Top right panel: The central peak provides a good estimate of a period which can then be used to seed a sine fit to the data yielding $f = 22.51981(3) \text{ d}^{-1}$. Bottom panel: A plot of the data folded at twice the the best-fit period with a sinusoidal fit superimposed. In this case $P_{\text{orb}} = 2/f$ due to ellipsoidal modulation although the corresponding frequency (11.2599 d^{-1}) is barely visible in the periodogram. This can be seen in the bottom panel with the deep eclipse of the white dwarf by the donor at $\Phi \approx 0.5$ and the two peaks at 0.25 in phase either side. In this case there is no doubt which is the correct alias but more generally the period uncertainty has to take account of the possibility of an incorrect alias being selected.

in the periodogram. The photometric orbital modulation of CVs can have various potential causes. Eclipses may occur once (of the white dwarf) or (rarely) twice (of the white dwarf and the donor, e.g. Ashley et al. 2020) per orbital cycle whilst ellipsoidal modulation due to the deformed shape of the donor star will yield two peaks per orbital cycle. Cyclotron beaming is another case where the waveform may show multiple peaks per orbital cycle, as does the emission from two poles in magnetic CVs.

Knowledge of the period assists the classification; SU UMa and ER UMa CVs typically have $P_{\text{orb}} \lesssim 3 \text{ h}$ (Ritter & Kolb 1998), WZ Sge have even shorter periods whilst U Gem and Z Cam CVs typically have $P_{\text{orb}} \gtrsim 3 \text{ h}$.

Whilst some periodograms show an unambiguous period others leave room for doubt due to aliases and harmonics, we have indicated such periods with a colon (:).

4.2.3 Hertzsprung–Russell and Colour–Colour Diagrams

The position of a CV on the Hertzsprung–Russell (HR) diagram aids classification as many CV types congregate in specific sections of the diagram (see Fig. 15 in Abril et al. 2020 and fig. 8 in

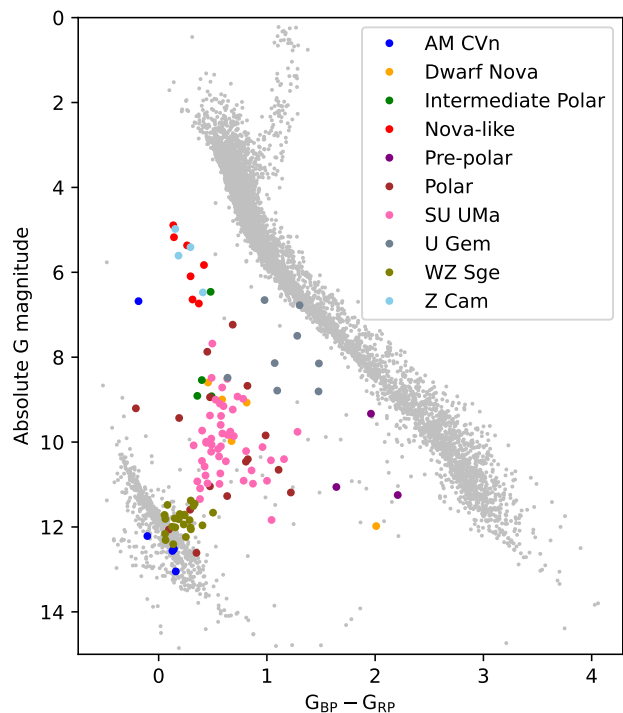


Figure 15. HR diagram showing all the CVs from SDSS I to IV where the astrometric and photometric errors are less than 10 per cent. The grey background consists of those *Gaia* objects closer than 100 pc with *GALEX* observations to increase the proportion of white dwarfs (which are UV-bright). Note the concentration of AM CVn and WZ Sge CVs near the white dwarf cooling sequence with SU UMa CVs spreading out towards the mains sequence. Novalike variables and Z Cam CVs are concentrated around $5 < G_{\text{abs}} < 7$ as their high \dot{M} results in large optical luminosity.

Inight et al. 2021). Absolute magnitudes require knowledge of the distance of a CV which is normally derived from *Gaia* parallaxes. Hence this diagnosis is not available for CVs without a *Gaia* counterpart. Even when *Gaia* data exists the position of a CV can be misleading if the parallax accuracy is poor or the CV is subject to significant reddening. A further issue is that CVs are intrinsically variable with outbursts, eclipses and orbital variations contributing to the observed spread in their distribution in the HR diagram. Fig. 15 shows a subset of the CVs from SDSS I to IV where systems with inaccurate parallaxes ($\varpi/\sigma_{\varpi} < 10$) or inaccurate magnitudes ($\text{phot_g_mean_flux_over_error} < 10$, $\text{phot_bp_mean_flux_over_error} < 10$, or $\text{phot_rp_mean_flux_over_error} < 10$) have been removed in line with Lindegren et al. (2018); Lindegren (2018). Inspection of Fig. 15 shows that the location of a CV in the HR diagram can aid its sub-type classification. The HR diagrams, where available, are included as PNG files in the supplementary data.

Where a *Gaia* counterpart does not exist, or does not have a parallax, a colour–colour diagram based on SDSS photometry is an alternative (see Fig. 16). This is typically the case for faint ($m \gtrsim 20$) systems. These approaches are somewhat complementary as SDSS photometry saturates at $m \approx 15$ and is not available for bright CVs.

4.2.4 Imaging

Pan-STARRS (Chambers et al. 2016) cutout images for each CV were obtained from the PS1 Image Cutout Server at STScI

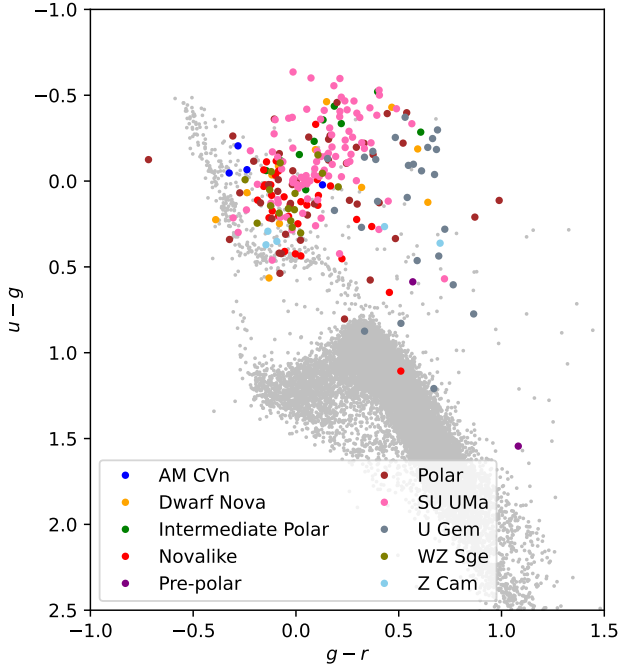


Figure 16. Colour-colour diagram showing the CVs from SDSS I to IV which have reliable SDSS photometry (where the magnitude of each colour is greater than 15.5 to avoid saturation and the magnitude error is less than 0.05). The grey background shows a collection of spectroscopically observed SDSS stars to guide the eye. The dense lower area forms the main sequence and the upper area is the white dwarf cooling sequence. Note the concentration of SU UMa and WZ Sge CVs on and above the white dwarf cooling sequence.

(Flewelling et al. 2020). We superimposed circles for each *Gaia* object (with the radius being proportional to the *Gaia* *G*-band magnitude) and for the SDSS fibre (2 arcsec diameter) (Fig. 17). The resulting image shows whether there is potential contamination of a spectrum from neighbouring objects, nebulae or background galaxies. In addition we superimposed circles for any *GALEX* detections. CVs often have *GALEX* observations but the accuracy of the coordinates of *GALEX* observations can be incorrect by a few arcseconds and the image helps to assess whether a *GALEX* observation could be associated with a different object. These images are available as PNG files in the supplementary data.

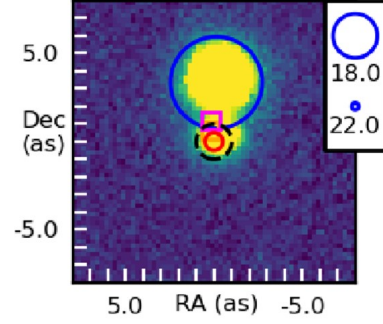


Figure 17. Pan-STARRS cutout of J0752+3628 showing the potential for the contamination of fibre spectroscopy. J0751+1444 has an apparent *Gaia* magnitude $m_G = 20.0$ whereas its neighbour, at a distance of 3.35 arcsec, has $m_G = 16.4$. The red circle denotes the target, the black dotted circle denotes the nominal coverage of an SDSS fibre (2 arcsec) and the blue circle is centred on the *Gaia* coordinates of the neighbour scaled according to the *Gaia* *G* magnitude. The *Gaia* coordinates are based upon EDR3 with an epoch of 2016 whilst the Pan-STARRS epoch is around 2012 and so a lack of alignment is a prompt to check proper motions to see if the contaminant was closer when the spectrum was observed. The pink square shows a *GALEX* observation.

Table 1: CVs from SDSS I to IV. We provide the geometric distances from [Bailer-Jones et al. \(2021\)](#) and CV sub-types according to the definitions in section 3. SDSS *g*-band magnitudes are from data release 7 ([Abazajian et al. 2009](#)). The references for the initial discovery (ID), spectrum (Sp) and orbital and superhump periods (*P* – where known) are also shown. New discoveries, orbital periods and sub-type identifications are shown in blue. Sub-type identifications in black are from VSX ([Watson et al. 2017](#)). : Tentative values, * Superhump periods, †low accretion SU UMa, ‡CVs with unusual state changes, §period bouncers. This is a short extract of the table, the full data is included in the supplementary data.

SDSS	Name	Gaia EDR3 source_id	<i>P</i> (h)	SDSS <i>g</i> (mag)	Distance (pc)	CV Sub-type	References		
							ID	Sp	P
J000014.74+255603.1				22.17		CV:	1	1	
J000720.77+200721.6	CSS 110921:000721+200722			21.48		WZ Sge:	15	1	
J000844.32-014014.6	Gaia15abi	2544817841421994624		17.93	1236 ⁺²²⁰ ₋₂₃₀	NL:/Polar	15	1	
J001107.26+303235.9	V0402 And	2861506395998660096	0.063499(3)*	20.4	793 ⁺⁴³⁴ ₋₂₂₅	SU UMa	11	1	5
J001153.08-064739.2	SDSS J001153.08-064739.1	2443219535337313280	0.10028081(8)	17.83	477 ⁺²⁹ ₋₁₉	U Gem	6	6	6
J001158.28+315543.7	CSS 101111:001158+315544	2861949606559861120	0.0554(1):	21.85		SU UMa	15	1	1
J001231.54+280011.1		2859847683924640384		20.98		WZ Sge:	1	1	
J001538.25+263656.7	CSS 090918:001538+263657	2856493142666940544	0.10150(6)	17.92	557 ⁺³⁶ ₋₃₄	SU UMa	15	7	7
J001856.92+345444.2	V0479 And	2876157251000218496	0.594093(4)	17.46	2027 ⁺⁴⁰⁸ ₋₂₅₉	Polar:	4	4	8
J002049.51+280020.2	MASTER OT J002049.54+280020.5	2857063063352792320	0.05658(1)	19.64	347 ⁺⁵⁹ ₋₄₅	WZ Sge:	13	1	1
J002243.55+061002.7	MGAB-V295	2747622177049417344	0.079(1):	19.88	2113 ⁺¹⁵⁹⁶ ₋₇₁₅	SU UMa	9	1	1
J002500.17+073349.2	CSS 081123:002500+073350	2748173586426407424		19.68	1484 ⁺⁴¹² ₋₃₀₆	DN/IP:	15	1	
J002637.05+242915.6	CSS 091026:002637+242916	2807191999055199232	0.08533(1)	18.75	588 ⁺¹⁰⁰ ₋₈₇	Polar	15	1	1
J002728.00-010828.5	EN Cet	2541910801397761152	0.05933(5)	20.78	1218 ⁺⁴⁶¹ ₋₅₄₇	WZ Sge	10	4	2
J002842.53+311819.4		2859593555004235520	1.217(1)	18.59	3642 ⁺¹¹⁵² ₋₉₈₅	NL	3	3	1
J002910.96+324125.8				22.12		DN	1	1	
J003151.76+202051.0	MGAB-V534	2796463449923353856	0.080871025(2)	18.06	368 ⁺¹⁹ ₋₁₆	SU UMa†	9	1	14
J003153.46+084118.5	ASASSN-17kg	2749846901389046656	0.0585(3)*	19.15	283 ⁺²⁴ ₋₁₇	WZ Sge	12	1	16
J003203.62+314510.4	CSS 091220:003204+314510	2859621764350006784		19.1	960 ⁺³³⁵ ₋₁₈₄	SU UMa	15	1	
J003459.90+273619.0	CSS 081031:003460+273620	2857545615813275136	0.07337(1)	21.12	1349 ⁺⁸²⁸ ₋₄₆₂	SU UMa	15	1	1

References: 1 [This work](#), 2 [Dillon et al. \(2008\)](#), 3 [Hou et al. \(2020\)](#), 4 [Szkody et al. \(2005\)](#), 5 [Kato et al. \(2012\)](#), 6 [Rebassa-Mansergas et al. \(2014\)](#), 7 [Thorstensen et al. \(2016\)](#), 8 [González-Buitrago et al. \(2013\)](#), 9 [MGAB catalog](#), 10 [Esamdin et al. \(1998\)](#), 11 [Antipin \(1998\)](#), 12 [Kepler et al. \(2015\)](#), 13 [Gentile Fusillo et al. \(2019\)](#), 14 [VSNET23583](#), 15 [CRTS candidate CV](#), 16 [VSNET21317](#)

5 RESULTS

In the interests of brevity the full observational data and analysis of the over 500 SDSS I to IV CVs has been consigned to the supplementary data. Illustrative examples are given here (Table 1 and Fig. 18) together with a brief discussion of a small set of the most interesting systems. Spectra have been smoothed by using a box-car median filter of width five points. A list of the 70 newly discovered CVs is included in Table A1.

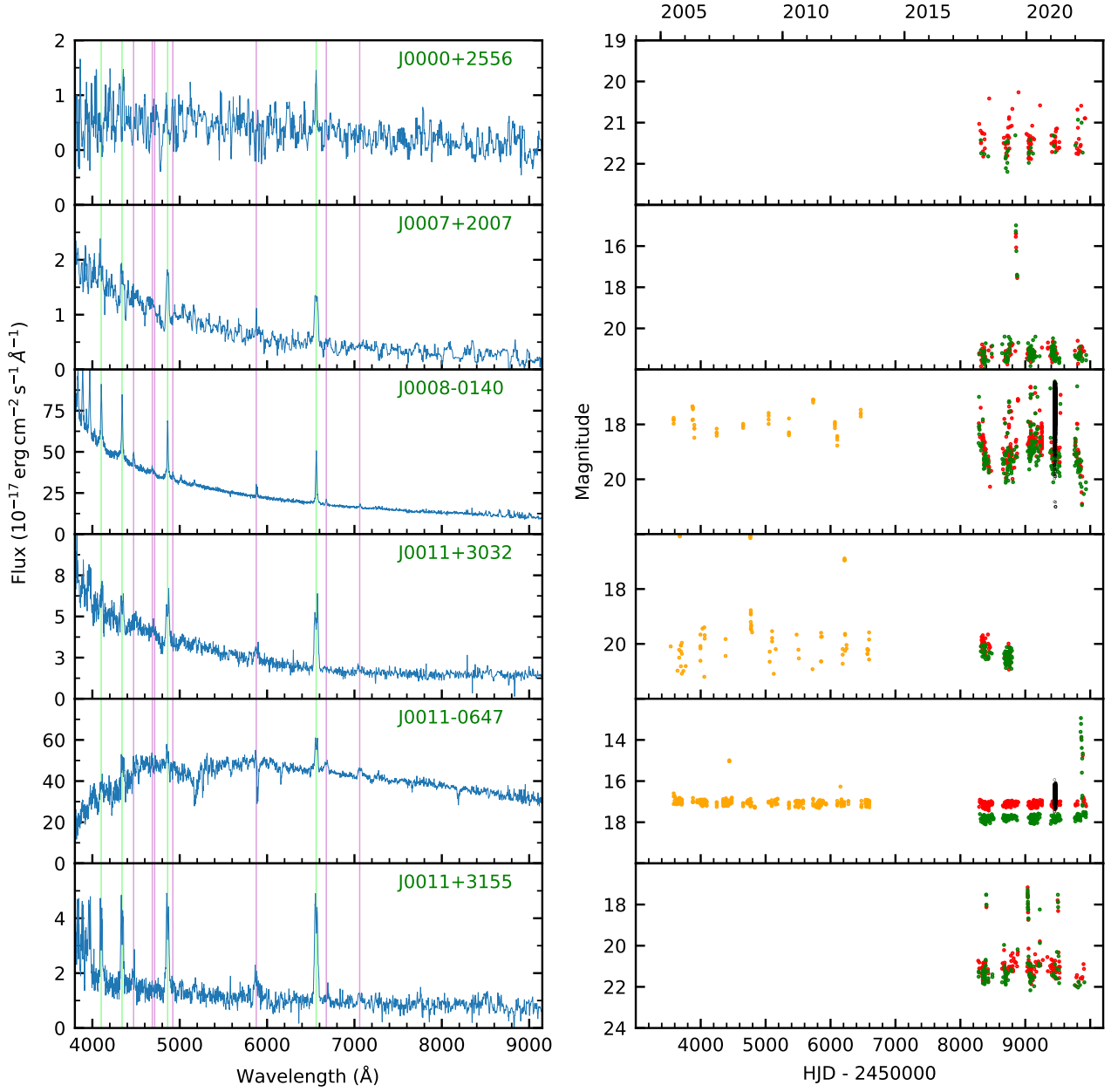


Figure 18: Left panels: Spectra with Balmer lines shown in green and He lines in pink. Right panels: Light curves with CRTS shown in orange, ZTF in red (r -band) and green (g -band) and *TESS* in black. This is a short extract of the data: the complete set is included in the supplementary data.

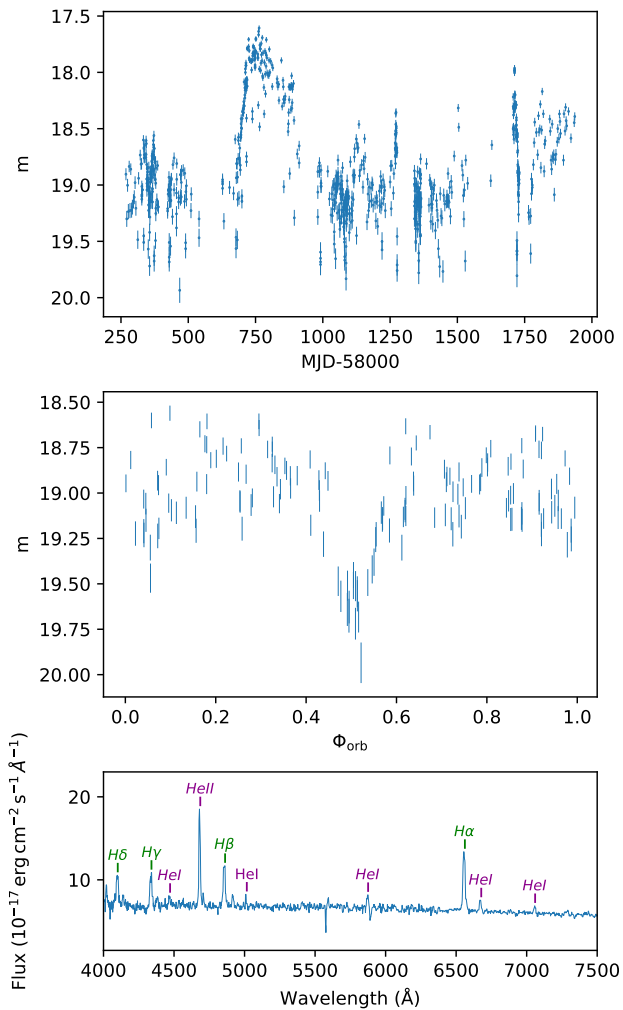


Figure 19. J0028+3118 is an eclipsing CV with an unusually long orbital period. Top panel: ZTF light curve (*r*-band) showing a brightening event lasting about one year. Middle panel: The section of the light curve with MJD < 58600 folded on the 29.2 h period. Bottom panel: SDSS spectrum with a prominent He II 4686 Å emission line.

5.1 Unusual systems

The following notes discuss a small selection of the systems in SDSS I to IV which have unusual features and are worthy of further study.

5.1.1 J0028+3118

The spectrum displays single-peaked Balmer emission lines above a flat continuum as well as a very strong He II 4686 Å emission line. The system is located close to the main sequence in the HR diagram. There is a ≈ 1 yr state change of ≈ 2 magnitudes at MJD ≈ 58750 together with three shorter and smaller brightening events in the ZTF light curve. The ZTF light curve (Fig. 19) suggests that $P_{\text{orb}} = 29.20(1)$ h and also that the system is eclipsing. J0028+3118 is a high-accretion novalike system but the very long period is unusual. The extraordinarily strong He II 4686 Å suggests a hot and helium-rich accretion stream – possibly the result of a hydrogen depleted donor that is still burning (Harrison 2018).

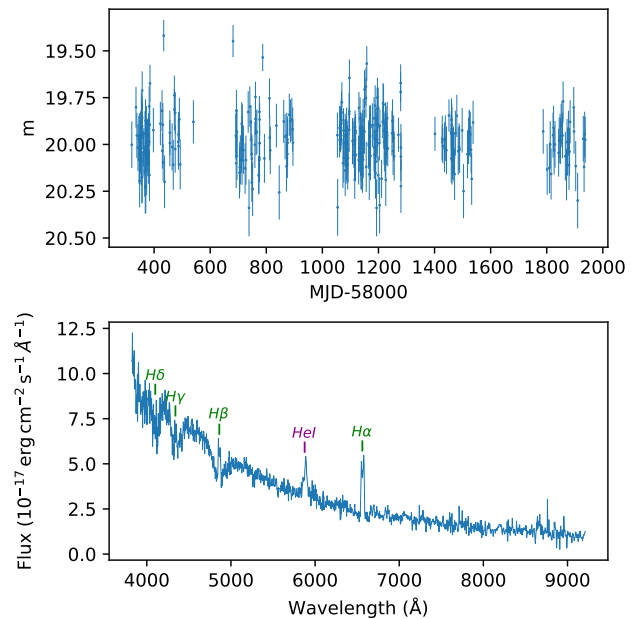


Figure 20. J0223–0520 is a CV with an unusually hot white dwarf. Top panel: ZTF light curve (*r*-band) showing variability. Bottom panel: SDSS spectrum showing the white dwarf absorption lines.

5.1.2 J0223–0520

The spectrum shows double-peaked Balmer emission lines with the higher order ones embedded in broad absorption lines from the white dwarf (Fig. 20). The blue slope of the continuum, and the shape of the white dwarf absorption lines suggest a relatively high white dwarf temperature, which is consistent with the SED being dominated by the white dwarf. The system is brighter in the far-ultraviolet (*GALEX* $m_{\text{FUV}} = 19.5$) than in the optical ($m_g = 19.9$). This is not consistent with its position at the lower end of the white dwarf cooling sequence in the HR diagram with $G_{\text{BP}} - G_{\text{RP}} = 0.35$, which would imply a temperature $T_{\text{eff}} \approx 8000$ K. The ZTF light curve shows variability but does not reveal an orbital period. There is an *XMM* X-ray detection which is unusual for a low- \dot{M} system (Webb et al. 2020). This is probably a WZ Sge. It is possible that the raised temperature of the white dwarf is the consequence of a previous eruption.

5.1.3 J0932+4725 and J0947+4524

Double-peaked Balmer, He I, He II and Ca emission lines are visible in the SDSS spectra of these systems as well as the Balmer jump in emission (Fig. 21). There is deep central absorption in the emission lines suggesting that they are eclipsing – which is confirmed by Homer et al. (2006) for J0932+4725, and by the ZTF light curve for J0947+4524. Both are closer to the white dwarf cooling sequence than the main sequence in the HR diagram. In the CRTS and ZTF light curves J0932+4725 exhibits outbursts and superoutbursts whilst J0947+4524 exhibits two small ($\Delta m \approx 1$) outbursts. J0932+4725 has a period of 1.588 h (Homer et al. 2006) whilst we obtained a period of 1.34963(2) h from the ZTF light curve.

The large ratio of the helium to hydrogen line strengths suggests that the donor is likely to be He-enriched. An *HST* observation of J0932+4725 by Pala et al. (2017) shows a large N v/C iv line flux ratio. Gänsicke et al. (2003) attribute this type of nitrogen excess to a system having passed through a phase of thermal timescale

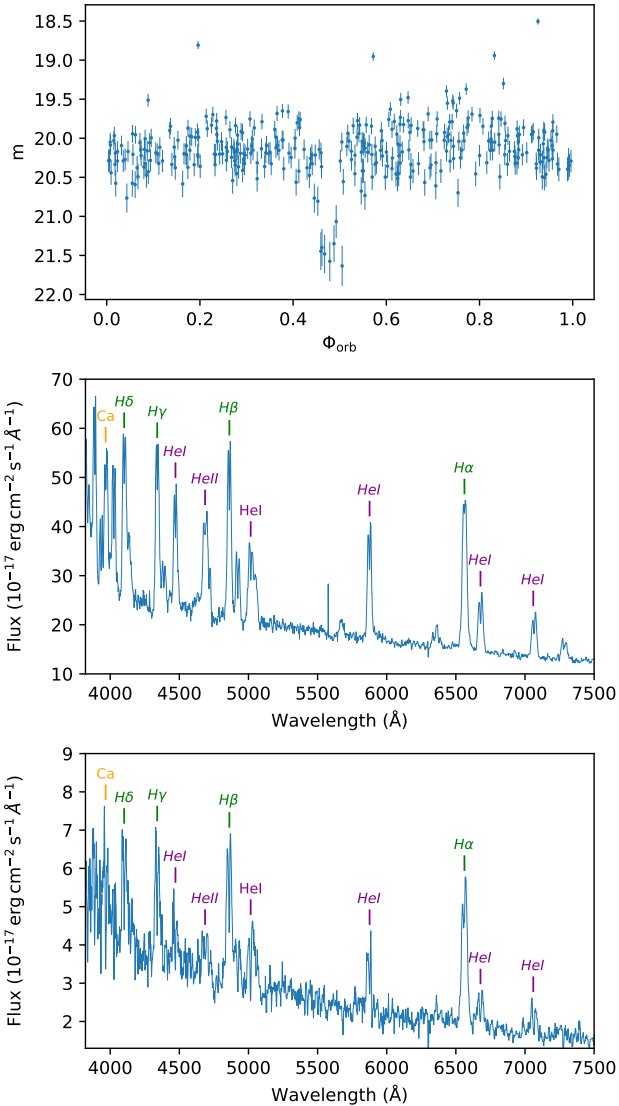


Figure 21. Two eclipsing CVs with unusually strong He I emission lines, which very likely contain stripped nuclear evolved donor stars. Top panel: Folded ZTF light curve of J0947+4525 showing eclipse. Middle panel: Spectrum of J0932+4725. Bottom panel: Spectrum of J0947+4524.

mass transfer and now accreting CNO processed material from a donor stripped of its external layers. J0932+4725 is therefore most probably such an evolved system. Whilst there are no *HST* spectra of J0947+4524 the optical spectrum is very similar to that of J0932+4725 and suggests that this may also have an evolved donor. Systems with evolved donors are interesting as they are potential precursors to AM CVn systems (Podsiadlowski et al. 2003; Goliaš & Nelson 2015)

The superoutbursts confirm that J0932+4725 is an SU UMa CV. J0947+4524 is a dwarf nova but we cannot classify it more precisely.

5.1.4 J1146+6759

Double-peaked Balmer and He I emission lines are visible in the spectrum as well as the Balmer jump in emission. The donor is not detected. J1146+6759 is located midway between the main sequence and the white dwarf cooling sequence in the HR diagram. The

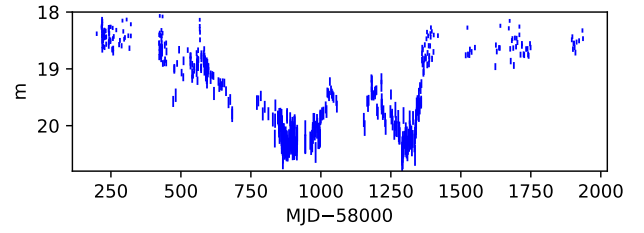


Figure 22. J1146+6759 has been classified as an SU UMa dwarf nova, but has an unusual ZTF light curve (r -band) showing a slow decline into a faint state without outbursts.

system was observed in a superoutburst on 2011 January 4 and a superhump period of 0.0615(8) d was reported (vsnet-alert 12567²), classifying this system as an SU UMa dwarf nova. The ZTF light curve shows very unusual variability (Fig. 22) with a steady decline in amplitude of $\Delta m \approx 1.5$ over three years. This is followed by a rapid return to the original magnitude and then an outburst. It demonstrates that some dwarf novae can undergo state changes (section 6.6)

5.1.5 J1150+4041

The spectrum shows strong Balmer, He I and He II asymmetric emission lines, suggesting that this is a magnetic CV. Neither the white dwarf nor the donor are visible. The ZTF light curve shows continuous variability with an amplitude of $\Delta m \approx 1$, but no outbursts. The periodogram computed from the ZTF data shows a clear and strong signal at an unusually long period of 141.65(5) h, or 5.9 d (Fig. 23). If this signal is genuinely the orbital period of the system, it would exceed that of the current record of 5.7 d (V1017 Sgr, Sekiguchi 1992). However, in contrast to V1017 Sgr, the spectrum of J1150+4041 does not reveal any signature of a donor star, normally detected at such a long orbital period. Moreover, the system is located relatively close to the white dwarf cooling sequence in the *Gaia* HR diagram, i.e. intrinsically faint. We have currently no consistent explanation for the observed properties of J1150+4041, but speculate that the long period might be the beat between the white dwarf spin and the orbital period in a slightly asynchronous polar. Radial velocity and fast photometry follow-up is required to unravel the true nature of this system.

5.1.6 J1224+1841

The spectrum shows a blue continuum with Balmer emission lines, which are embedded in Balmer absorption lines for H β and the higher Balmer lines. J1224+1841 is located in the area of the HR diagram occupied by novalike variables. The ZTF light curve shows multiple outbursts and also a drop of $\Delta m \approx 2$ to a low state lasting several hundred days (Fig. 24). There appear to be outbursts during the low state although it is possible that they are very short reversions to the high state. The CRTS light curve shows two similar low states. J1224+1841 belongs to the growing family of CVs bordering between novalike variables and dwarf novae (Kato 2019; Kato et al. 2021; Inight et al. 2022). Radial velocity follow-up should be carried out to determine the orbital period of this system.

² <http://ooruri.kusastro.kyoto-u.ac.jp/mailarchive/vsnet-alert/12567>

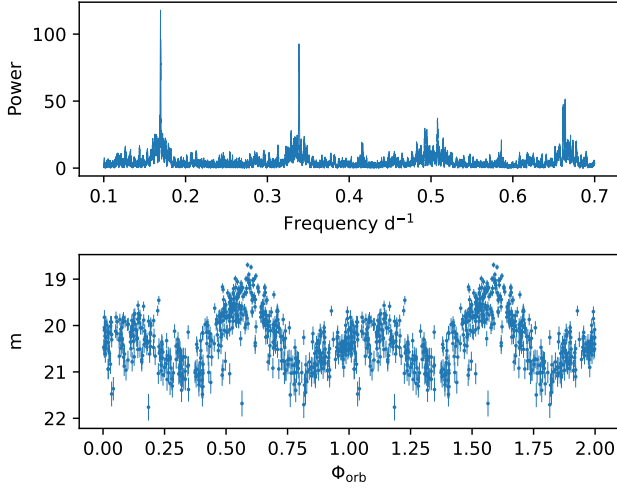


Figure 23. The ZTF data of J1150+4041 shows a very clear and strong signal at an unusually long period of 141.65(5) h. The highest peak in the periodogram from the ZTF light curve is the second harmonic and the folded light curve shows a double humped profile.

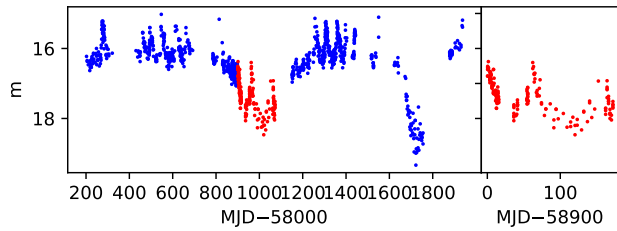


Figure 24. J1224+1841 is a transitional object between novalike variables and dwarf novae: the ZTF light curve shows both outbursts and a drop-out (red). Outbursts also appear to occur during the faint state.

5.1.7 J1244+5936

This system is also known as Gaia16adi (Wyrzykowski et al. 2012). A double-peaked $H\alpha$ emission line is visible in the spectrum as well as other Balmer, He I and He II emission lines (Fig. 25). The deep central absorption features in the higher Balmer lines, dipping below the continuum flux level, suggest that the system is eclipsing, which is confirmed by the ZTF photometry. Absorption lines from the white dwarf are visible together with TiO molecular bands from the donor. It is closer to the white dwarf cooling sequence than the main sequence in the HR diagram. The ZTF and CRTS light curves show ≈ 10 outbursts with at least one low amplitude superoutburst accompanied by superhumps. We obtained a reliable period of 1.74954(1) h from the ZTF light curve and a consistent period from the CRTS light curve. The folded light curve shows that it is eclipsing with a hot spot just before the eclipse. J1244+5936 appears to be an SU UMa albeit with a very low \dot{M} . It may have recently started accreting – possibly after passing through the period gap; although theory (D’Antona et al. 1989) suggests that this transitional period will be short ($\sim 10^6$ yr).

5.1.8 J1522+3913

The spectrum (Fig. 26) shows Balmer emission lines above a relatively red continuum. Narrow absorption lines reveal a \approx G-type donor star. The SED of the system exhibits a clear ultraviolet excess

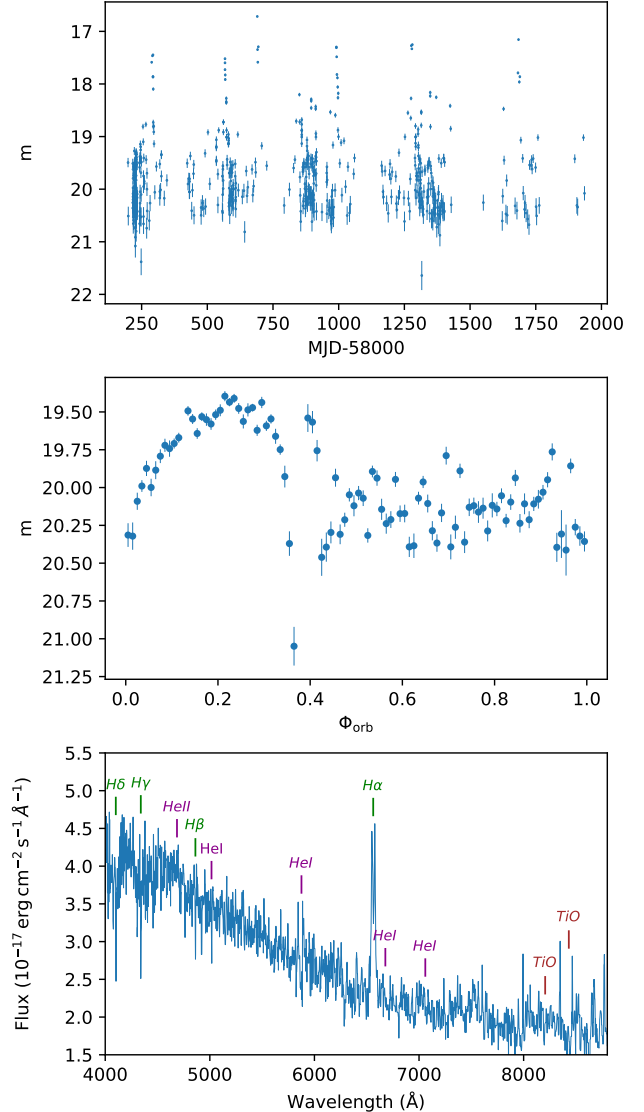


Figure 25. J1244+5936 (Gaia16adi) is an eclipsing system with a very low accretion rate. Top panel: ZTF light curve (r -band). Middle panel: Light curve folded at the orbital period of 1.75 h, and rebinned into 30 phase bins. Note the eclipse of the disc at $\Phi_{\text{orb}} \approx 0.4$ and the eclipse of the hot spot at $\Phi_{\text{orb}} \approx 0.45$. Bottom panel: SDSS spectrum showing $H\gamma$ and $H\delta$ absorption lines from the white dwarf and TiO absorption lines from the donor in the red.

in the *GALEX* bands, most likely from the accretion disc. The *Gaia* HR diagram shows that J1522+3913 is just evolving off the main sequence into the giant branch. The ZTF light curve shows at least one outburst. We obtained a reliable period of 10.7686 d (258.4464 h) from the ZTF light curve confirming the period found by Drake et al. (2014) from the CRTS data. The folded light curve shows a clear double hump, consistent with the detection of ellipsoidal modulation. To our knowledge J1522+3913 is the longest known orbital period for a CV – twice that of V1017 Sgr ($P_{\text{orb}} = 5.714$ d, Sekiguchi 1992). We note that a small number of symbiotic stars are located in this region of the HR diagram as well, however, J1522+3913 does not show any of the defining features in its spectrum (see the definition in section 1.1 of Merc et al. 2021). Instead, we suggest that the very long orbital period, and the location in the HR diagram are consistent with a CV in which the donor has evolved

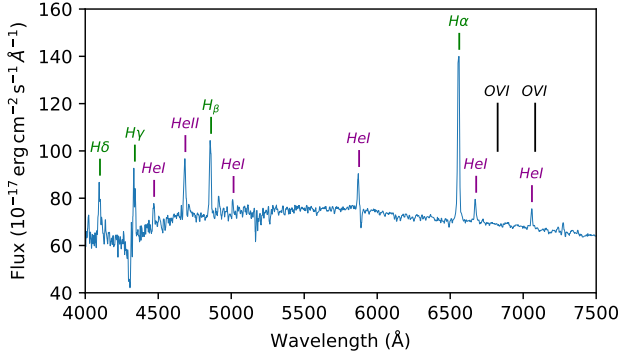


Figure 26. The spectrum of the long-orbital period (10.8 d) J1522+3913 contains narrow absorption features from a G-type donor. The helium emission lines suggest that the donor is evolved. There are no molecular and metallic absorption lines or Raman-scattered O VI lines; two of the conditions in Merc et al. (2021) for a symbiotic star classification.

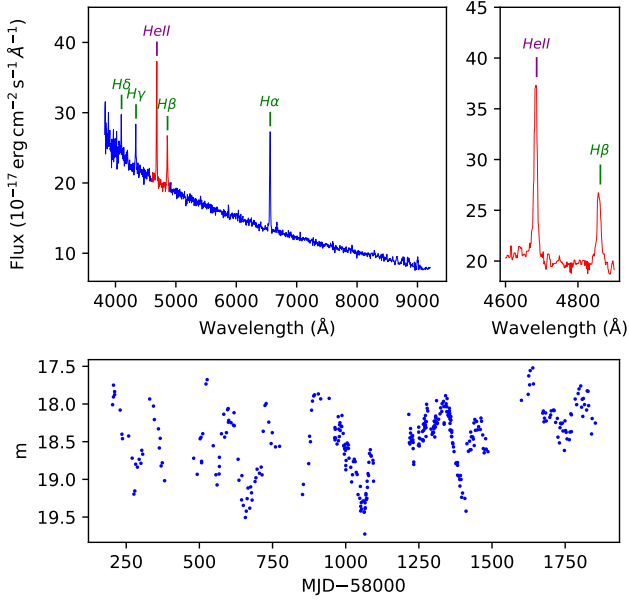


Figure 27. J1549+1739 is probably a novalike variable. Top panel: The spectrum shows an unusually strong He II line. Top inset panel: Expanded plot of the He II line. Bottom panel: The ZTF light curve (*r*-band) shows repeated changes of magnitude on timescales of about a year.

off the main sequence (e.g. for example GK Per Álvarez-Hernández et al. 2021).

5.1.9 J1549+1739

The SDSS spectrum shows single-peaked Balmer emission lines and a very strong He II emission line on top of a strong blue continuum (Fig. 27). There is no sign of the white dwarf or the donor. J1549+1739 is located in the novalike variable area of the HR diagram. Whilst there are no outbursts in the CRTS and ZTF light curves, the system meanders on time scales of about a year between $m \approx 17.5 - 19$. This is probably a novalike variable but the strong He II and its light curve are unusual. Spectroscopic follow up is encouraged to explore the spectral changes between the bright and faint states, and to determine the orbital period of the system.

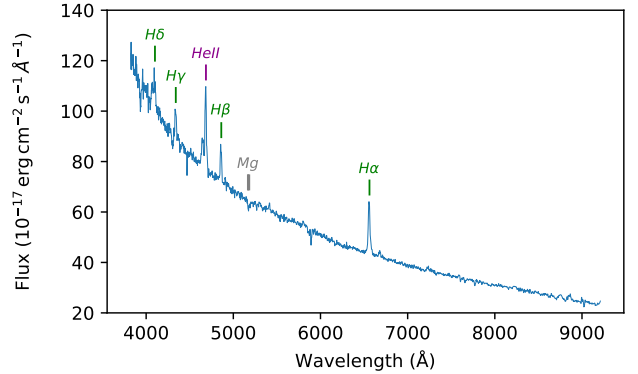
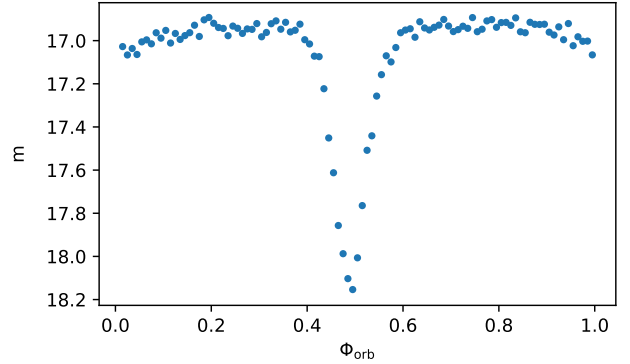
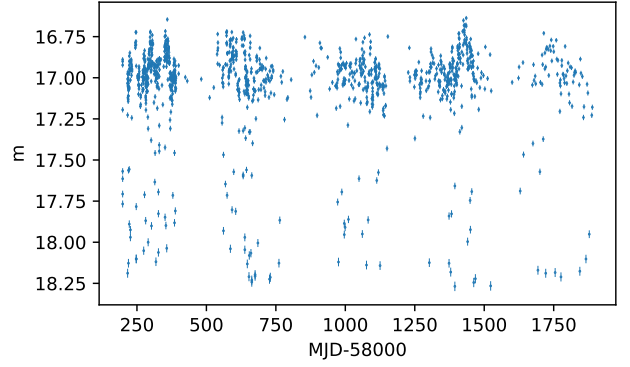


Figure 28. J1712+3218 is a novalike variable with an unusually long orbital period. Top panel: ZTF light curve (*r*-band) showing eclipses. Middle panel: ZTF light curve folded on 8.96 h showing the eclipse. Bottom panel: The spectrum shows absorption lines that may be from an early-type donor (Mg is indicated).

5.1.10 J1712+3218

The spectrum (Fig. 28) shows Balmer and Helium emission lines, including strong He II, and the Bowen blend above a blue continuum. Narrow absorption lines of Mg, Na and Ca are detected, which may be from the donor star. J1712+3218 is located in the novalike variable area of the HR diagram. The ZTF light curve shows variability with clear eclipsing behaviour. Drake et al. (2014) report an orbital period of 17.998 h and concluded that this is a Beta Persei system. We determine $P_{\text{orb}} = 8.9599(1)$ h from the eclipses in the ZTF light curve. We also have unpublished MDM time series spectroscopy confirming the orbital period. We classify J1712+3218 as a novalike variable. This is an unusually long period for a novalike variable although it would be consistent with an early donor that is visible even though the disc is in a high state.

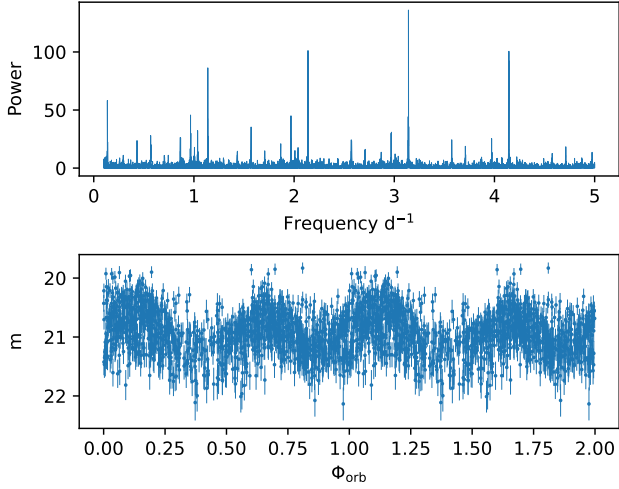


Figure 29. J1726+5432 has an unusually long period of $P_{\text{orb}} = 15.2783(3)$ h. Top panel: The periodogram peak at 3.14 per day is at twice P_{orb} . Bottom panel: Light curve folded at P_{orb} .

5.1.11 J1726+5432

This system has two SDSS spectra obtained at MJDs 51813 and 51997. Both spectra show single-peaked Balmer, He I and He II emission lines as well as the Balmer jump in emission (Fig. 29). The SED shows that it has historically been brighter. There is no *Gaia* parallax. It is above the white dwarf cooling sequence in the SDSS $u - g, g - r$ diagram, although the SDSS photometry was obtained during a brighter state. The ZTF light curve shows no outbursts but low-level variability. We find an unusually long period of 15.2783(3) h from the ZTF light curve which, together with the helium-rich spectrum may indicate an evolved donor. In the absence of outbursts we cannot assign a sub-type and have classified this generically as a CV.

5.1.12 J1831+4202

He I absorption lines are detected in the spectrum superimposed on a blue continuum (Fig. 30). There is no sign of the white dwarf or the donor. J1831+4202 has previously been classified as a CV (Girven et al. 2011) and a DB white dwarf (Genest-Beaulieu & Bergeron 2019; Geier et al. 2019a) however the DB classification is inconsistent with the variability in the *Gaia* and ZTF light curves which indicates that this is an interacting binary. It is close to AM CVn in the HR diagram and we hence classify this system as an accretion-disc dominated AM CVn. The drop-outs in the *Gaia* and ZTF light curves are unusual for this type of system.

5.1.13 J2119+0332

Double-peaked Balmer and He I lines are visible in the spectrum as well as the Balmer jump in emission (Fig. 31). There are also Na absorption lines at $\approx 8190 \text{ \AA}$ and at $\approx 5890 \text{ \AA}$ together with broad Mg at $\approx 5170 \text{ \AA}$ suggesting a K-type donor. J2119+0332 is closer to the main sequence than the white dwarf cooling sequence in the HR diagram. There are no outbursts in either the CRTS or the ZTF light curves. We found ellipsoidal modulation and a reliable orbital period of 2.37223(3) h from the ZTF light curve, i.e. within the period gap. The period and relatively low luminosity are inconsistent with a main-sequence K-type donor and reminiscent of

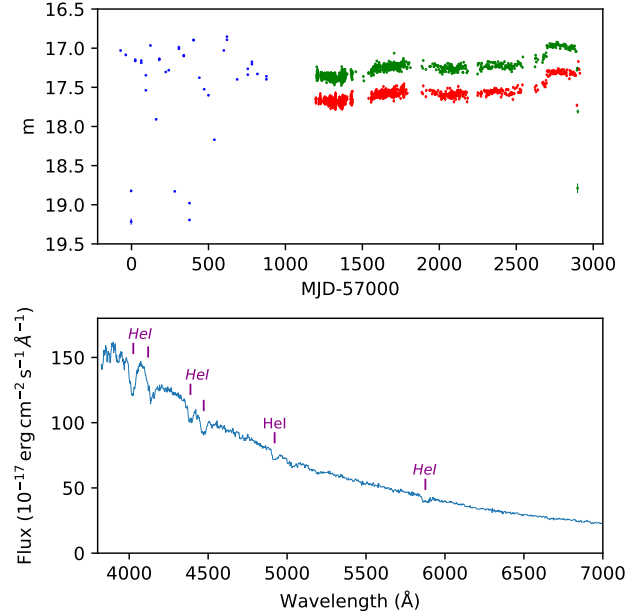


Figure 30. J1831+4202 is an AM CVn with a helium-dominated absorption line spectrum and it exhibits low-amplitude brightness variations on time scales of about a year with occasional drop-outs. Top panel: The ZTF light curve (r - and g -band data shown in red and green respectively) and the *Gaia* light curve (shown in blue). Bottom panel: Spectrum showing helium absorption lines and an absence of hydrogen lines.

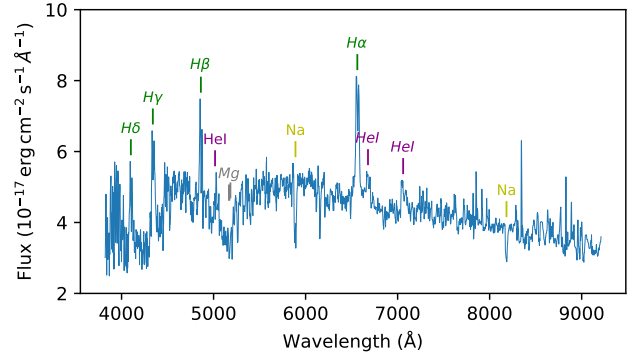


Figure 31. The spectrum of J2119+0332 shows Na and Mg lines consistent with a K-type star. Whilst bright enough to outshine the disc the spectrum is too dim for a main sequence K-type suggesting a nuclear evolved stripped donor. This hypothesis is corroborated by the short orbital period of 2.4 h.

SDSS J001153.08–064739.2 (Rebassa-Mansergas et al. 2014) and QZ Ser (Thorstensen et al. 2002a) where the donor has undergone nuclear evolution on the main sequence before mass transfer to the white dwarf commences. In these cases a period of rapid mass transfer has resulted in a stripped donor and a short period. The strong Na absorption lines are consistent with CNO burning.

5.2 Non-CVs

The classification of a number of systems that were previously classified as CVs have now, with the benefit of new data such as from *Gaia* and ZTF, been revised. Most of the systems previously classified as CVs turned out to be either single white dwarfs or white dwarf plus main sequence binaries, in which emission lines from

a nebular background or from the chromosphere of the companion were mistaken for signatures of accretion flows. The new classifications of these non-CV systems are listed in Table 2.

6 DISCUSSION

6.1 Distribution of periods

We have assembled periods for over half of the CVs in SDSS I to IV, either from the literature or from our analysis of the ZTF data. The main reasons why the remaining systems have no period measurements are either a low inclination (which will reduce the amplitude of any orbital modulation), faintness (i.e. low signal-to-noise ratio of the time-series photometry or spectroscopy), or sparse sampling of the available time-series data. With the possible exception of low \dot{M} short-period CVs (which do not have much orbital modulation from the hot spot and are inherently fainter) these factors are not likely to correlate with the period. The distribution of the SDSS CV periods is therefore assumed to be relatively unbiased, which we compare in Fig. 32 with that of version 7.24 (December 2015) of the Ritter & Kolb (2003) catalogue of CVs (hereafter R&K). This final version of the R&K catalogue lists 1429 CVs (including some from SDSS I to IV); however it focuses on well-studied CVs, many of which were discovered by virtue of their outbursts.

Interestingly the period gap is clearly evident in the period distribution of CVs from the R&K catalogue but is not so evident in the SDSS I to IV sample. The proportion of SDSS CVs with periods below three hours is also greater than in the R&K catalogue, presumably due to spectroscopic identification of CVs with infrequent outbursts as reported by Gänsicke et al. (2009), and the fact that the SDSS CV sample reaches, on average, fainter apparent magnitudes than the R&K sample (19.7 and 18.1 respectively). This is consistent with the results obtained by Pala et al. (2020) and Inight et al. (2021). Fig. 32 highlights that selection effects have to be taken carefully into account when constructing observed CV samples to develop, support, or disprove theories of CV evolution, such as the canonical “disrupted magnetic braking framework” (Rappaport et al. 1983; Knigge et al. 2011) as well as suggestions that the structure of the donor star may have no strong dependence upon the efficiency of magnetic braking (Andronov et al. 2003; El-Badry et al. 2022).

The orbital period distribution broken down by CV-sub-type is shown in Fig. 33. From the top panel it can be seen that U Gem CVs typically have periods above the period gap whilst most SU UMa CVs are located below the gap. Later in the evolution process low accretion WZ Sge CVs approach the period minimum and subsequently evolve back towards longer periods as “period bouncers”. The CVs below the period minimum have helium-rich donors which were partially evolved before accretion commenced or formed directly from a detached white dwarf/brown dwarf binary (Kolb & Baraffe 1999; Littlefair et al. 2007; Podsiadlowski et al. 2003). Polars tend to have shorter periods whilst those of intermediate polars and pre-polars tend to be longer. The “period gap” is not so apparent in magnetic CVs, (see for example Mason et al. 2019) and may be a result of less efficient magnetic braking due to the white dwarf magnetic field (Webbink & Wickramasinghe 2002). Novalike variables congregate above the period gap alongside classical novae. Many classical novae become novalike variables following their eruptions although there are exceptions where they become dwarf novae in the period between eruptions (Honeycutt et al. 1995; Mróz et al. 2016). Short-period novalike variables are very rare; BK Lyn is the most famous example: Patterson et al. (2013) speculate that this is

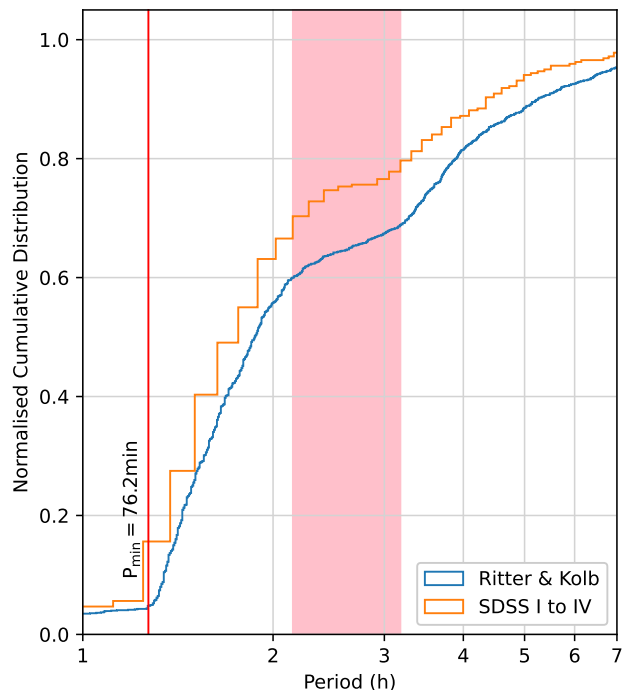


Figure 32. Cumulative distribution of the periods of the CVs in SDSS I to IV. The distribution is compared with that of the Ritter and Kolb catalogue (version 7.24, Ritter & Kolb 2003). The period minimum (red line) and “period gap” (pink rectangle) are identified (see text for details).

due to being the result of a relatively recent (~ 2000 yr ago) nova, and it has now morphed into an ER UMa dwarf nova.

The evolution of orbital periods of CVs across the HR diagram is shown in Fig. 34. CVs originate in or near the main sequence, with their luminosity dominated either by a luminous accretion disc or donor star, and progressively migrate towards the white dwarf cooling sequence as their donor mass decreases and periods shorten. In most WZ Sge the contribution of the accretion disc to their optical flux is small, and that of their donor stars entirely negligible.

6.2 Distribution of CV sub-types

The distribution of the SDSS I to IV CV sub-types is shown in Fig. 35, where we compare it with that of the 150 pc volume-limited sample (Pala et al. 2020) and also with that of the R&K catalogue.

The proportion of magnetic CVs (polars, pre-polars and intermediate polars) in our sample is 20 per cent which is consistent with the 18 per cent found in Ritter & Kolb (2003) but is much lower than the 34 per cent found in Pala et al. (2020). This may be due to the small sample size (42) in Pala et al. (2020) which has a statistical 2σ uncertainty of ± 19 per cent. By comparison our sample (507) has an uncertainty of ± 0.03 per cent. Alternatively the difference may be because the absolute luminosity of polars is on average lower than non-magnetic systems causing a selection effect in our magnitude-limited sample.

The proportion of novae and novalikes is lower in Pala et al. (2020) than our sample. This is due to their intrinsic brightness rendering them visible at far greater distances than other CVs and hence there will be a higher proportion in our magnitude-limited sample. The proportion is greater still in Ritter & Kolb (2003) due to historic novae identified by their eruptions.

We found a smaller proportion of WZ Sge CVs than Pala et al.

Table 2. Systems identified as CVs in the literature which we have reclassified as detached binaries or isolated stars. Unless otherwise stated the original classification was taken from [Szkody et al. \(2011\)](#). Each system may include a white dwarf (WD), M dwarf (M) or other type of main sequence star (MS).

SDSS name	Notes	New type
002603.80-093021.0	Thorstensen & Skinner (2012) determined that the spectrum was not that of a CV. Kleinman et al. (2013) classified the object as a (hydrogen) DA white dwarf. We found a ZTF period of 9.3086hh confirming that this is probably a binary.	WD+MS
034420.16+093006.8	Parsons et al. (2015) found that this is a detached, eclipsing system.	WD+MS
035409.32+100924.4	Kleinman et al. (2013) found that this was an eclipsing system including a DA white dwarf. This system is within the Eridanus superbubble (see fig. 1 in Ryu et al. 2006) and this is likely to be the source of the Balmer emission lines; the remaining spectrum is that of an isolated white dwarf.	WD
053659.12+002215.1	Thorstensen & Skinner (2012) determined that the spectrum was not that of a CV. Kleinman et al. (2013) classified the system as a DA white dwarf. This system is on the edge of the Eridanus superbubble (see fig. 1 in Ryu et al. 2006) and this is likely to be the source of the Balmer emission lines; the remaining spectrum is that of an isolated white dwarf.	WD
075117.09+144423.5	The spectrum shows emission lines but these are contamination from a nearby CV (PQ Gem) and the object is actually an M-dwarf.	MS Star
102347.67+003841.2	Wang et al. (2009) found that this object is a millisecond radio pulsar - a low mass X-ray binary including a neutron star.	Low mass X-ray binary
105443.06+285032.7	Rebassa-Mansergas et al. (2010) concluded that the object is a detached binary including a DA white dwarf. Thorstensen & Skinner (2012) also determined that the spectrum was not that of a CV. We note that the weak Balmer emission lines appear to vary in strength between multiple SDSS spectra.	WD+M
111703.53+182558.1	Thorstensen & Skinner (2012) determined that the spectrum was not that of a CV. We classify the system as a detached binary containing a hot white dwarf and a main sequence star. The SDSS and LAMOST (He et al. 2017) spectra show that the emission lines vary in strength consistent with coming from the irradiated secondary at different phases of the orbit. We find a period of 9.33 h from the ZTF light curve.	WD+MS
121929.46+471522.8	Gänsicke et al. (2020) concluded that this was an isolated magnetic white dwarf with Zeeman-split Balmer line emission.	WD
124959.76+035726.6	Rebassa-Mansergas et al. (2010) concluded that the object is a detached binary including a DA white dwarf. Thorstensen & Skinner (2012) also determined that the spectrum was not that of a CV. We find a period of 17.84 h from the ZTF light curve.	WD+M
130236.21+060148.0	Thorstensen & Skinner (2012) determined that the spectrum was not that of a CV. Kiman et al. (2019) found that it was an isolated system – either an M or L dwarf.	M/L dwarf
131424.68+455528.3	Kepler et al. (2016) identified this as a CV from SDSS data release 12. However the spectrum only shows very narrow emission lines and there are no recorded outbursts. It is in a nearby galaxy, UGC 8320 (4.3 Mpc, Karachentsev et al. 2003), and so it is most likely to be a hot star with the emission lines arising from the background galaxy.	MS Star
131709.07+245644.2	Thorstensen & Skinner (2012) determined that the spectrum was not that of a CV.	WD+M
132856.71+310846.0	Thorstensen & Skinner (2012) determined that the spectrum was not that of a CV. Geier et al. (2019b) found that it was a hot luminous subdwarf.	Hot luminous subdwarf?
151500.56+191619.6	Thorstensen & Skinner (2012) determined that the spectrum was not that of a CV. It appears to be a detached binary with emission lines caused by irradiation.	WD+MS
155904.62+035623.4	Thorstensen & Skinner (2012) determined that the spectrum was not that of a CV. Parsons et al. (2013) concluded that it was a WD+MS. We find a period of 2.5h from the ZTF light curve.	WD+MS
202520.13+762222.4	The spectrum is very noisy with only the H α emission line clearly visible. There are no recorded outbursts and it is on the main sequence. The SED is consistent with this being a single M-dwarf. This is most likely to be a flaring main sequence star rather than a CV.	MS Star
210241.09-004408.3	Thorstensen & Skinner (2012) determined that the spectrum was not that of a CV	MS Star or subdwarf?

(2020) most probably because they are inherently faint and only observed at relatively short distances.

6.3 Variability of CVs

The photometric variability of CVs is widely used as a selection criterion when searching for CV candidates. However, different CV sub-types display very different types of variability, both in terms of amplitude and time-scales, and hence specific variability selection methods may introduce strong biases towards (or against) individual sub-types.

To illustrate this point, we computed three variability criteria for the SDSS I to IV CVs: (1) The difference between the maximum and minimum magnitude over the full set of ZTF observations which will be sensitive to outbursts and eclipses, where we only included systems with at least 150 observations. (2) The reduced χ^2 of the ZTF photometry with respect to its median. (3) the *Gaia* G-band variability defined as ([Guidry et al. 2021](#))

$$G_{\text{var}} = \frac{\text{phot_g_mean_flux_error} \times \sqrt{\text{phot_g_n_obs}}}{\text{phot_g_mean_flux}} \quad (1)$$

The distribution of these three types of variability are shown in the *Gaia* HR diagram in Fig. 36).

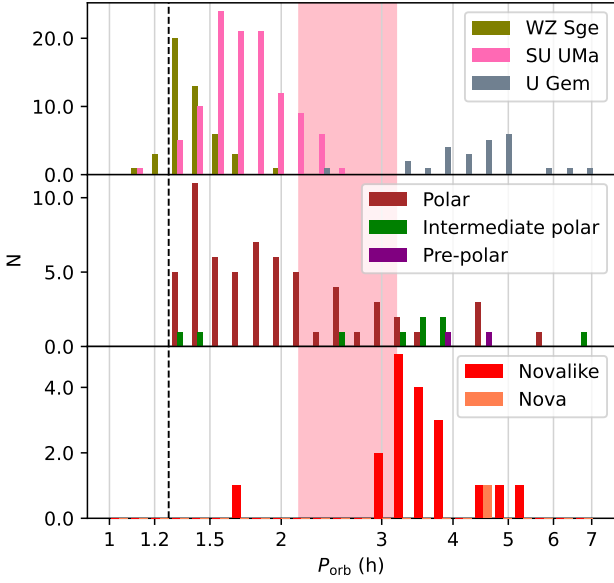


Figure 33. Distribution of the periods of the CV sub-types in SDSS I to IV. CVs evolve from right to left past the “period gap” (pink rectangle) to the period minimum (broken black line) and then back out to longer periods. Top panel: U Gem CVs typically have periods above the period gap whilst most SU UMa CVs have shorter periods below the gap. Middle panel: Polars tend to have shorter periods whilst intermediate polars and pre-polars tend to be longer. Bottom panel: Novalike variables congregate above the period gap alongside classical novae.

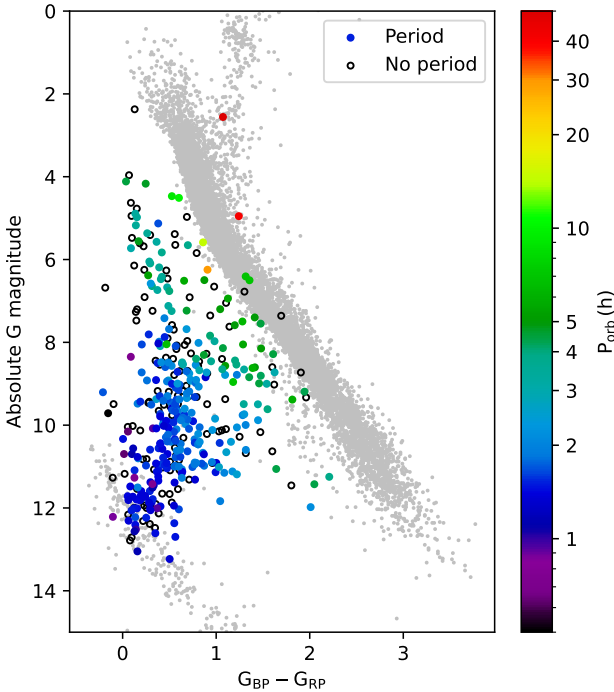


Figure 34. HR diagram of the CVs in SDSS I to IV showing the orbital periods where available. CVs without a period are shown as empty black circles. Note that the shortest periods are close to the white dwarf cooling sequence and the longest periods are close to the main sequence.

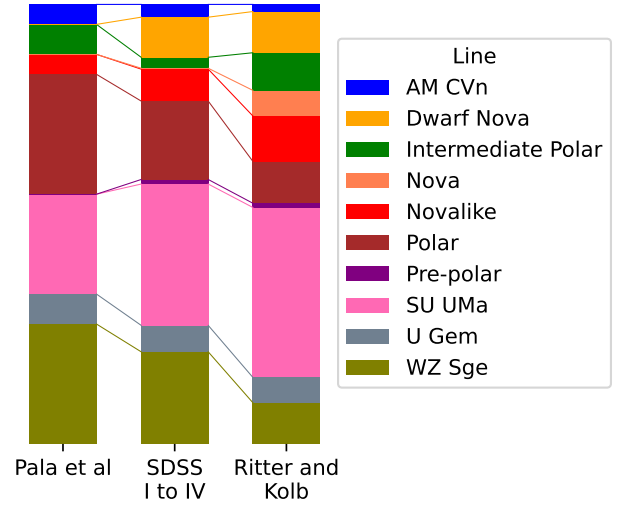


Figure 35. Comparison of the distribution of sub-types between a volume-limited 150 pc sample (Pala et al. 2020), the SDSS I to IV sample and the R&K catalogue. Objects identified as either CVs or magnetic CVs (30 out of 507 in SDSS I to IV) without further classification have been omitted in each case. Selection effects are clearly evident with faint and/or non-outbursting sub-types less common in the R&K sample. The proportion of magnetic systems is also significantly higher in the 150 pc sample.

The maximum amplitude of variability in the ZTF light curves (top panel) shows a concentration half-way between the white dwarf cooling track and the main sequence. This reflects the predominant population of SU UMa type CVs in this area of the HR diagram (see Fig. 15), which have frequent dwarf nova outbursts with amplitudes of $m \approx 3 - 5$, i.e. it is very likely that ZTF, despite the sparse sampling, will have caught them during an outburst. In contrast, the regions occupied predominantly by novalike variables ($G_{BP} - G_{RP} \approx 0.25$, $G_{abs} \approx 6$) and WZ Sge systems ($G_{BP} - G_{RP} \approx 0.25$, $G_{abs} \approx 12$) show only relatively small variations between the minimum and maximum brightness detected by ZTF. This is reflected by their stable, hot (novalike variables) or cool (WZ Sge CVs) accretion discs. However, a few systems in the region occupied by WZ Sge CVs show very large amplitude, $\Delta m \approx 8$, variability, implying that ZTF observed them during one of their rare super-outbursts. The ZTF reduced χ^2 diagram shows overall a similar trend, however, the area occupied by novalike variables exhibits a higher level of variability than in the maximum amplitude diagram, most likely because many of these systems have persistent short-term variability (flickering, Bruch 1992), and on average higher quality ZTF light curves as they are intrinsically bright. Finally, the *Gaia* variability diagram shows again a lack of variability in the area occupied by novalike variables and WZ Sge stars, and overall a lower number of strongly variable systems. This is most likely due to the fact that the *Gaia* data spans a shorter baseline (≈ 2.8 yr), and has on average less data points than the ZTF photometry. Future *Gaia* releases will extend the baseline to at least 5 yr, possibly up to 10 yr, increasing the diagnostic power of the *Gaia* variability index.

6.4 Space Density

Measuring the space density of the various CV sub-types is fundamentally important for validating evolutionary models.

Assuming that the Galaxy is axially symmetrical the space

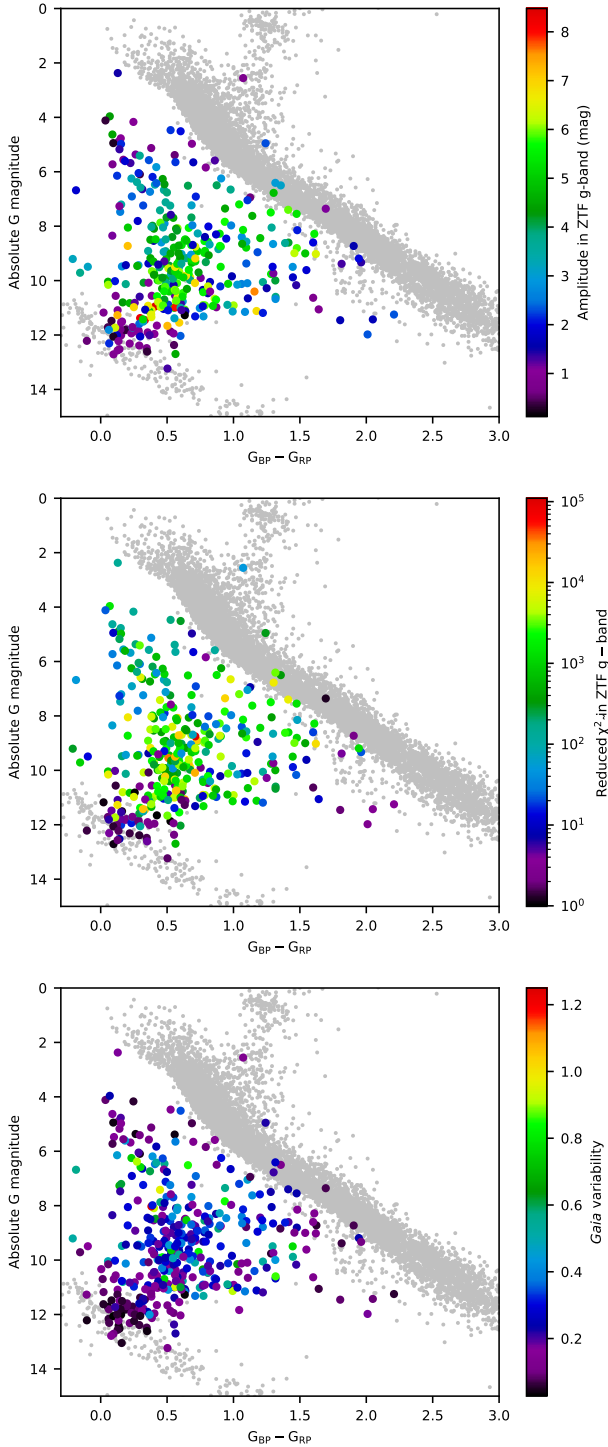


Figure 36. Variability of CVs related to position in the HR diagram. In each case older CVs which are approaching the white dwarf cooling sequence show less variability. Top panel: Distribution of maximum variability in the g -band ZTF light curve. Middle panel: Reduced chi-squared of the variability of the g -band ZTF light curve with respect to the median magnitude. Bottom panel: Variability in *Gaia* G -band magnitude (Eq. 1).

density of a class of objects is a function of the height above the Galactic disc and the radial distance from the Galactic centre. Our analysis is sufficiently local that radial variations will be small and we henceforth ignore this factor. We further assume an exponential vertical distribution with scale height h where h is assumed to be dependent upon the typical age of the CV sub-type. The space density at a height z above the plane is therefore:

$$\rho(z) = \rho_0 \times \exp\left(-\frac{|z|}{h}\right) \quad (2)$$

Our objective is to estimate the space density of the CV sub-types. Hence if the estimate of the number of a sub-type in a volume V is N_{obs} the space density is given by:

$$\rho_0 = \frac{N_{\text{obs}}}{\int_V \exp\left(-\frac{|z|}{h}\right) dv} \quad (3)$$

which for a suitably large sample volume would become a constant dependent only on the choice of h . This poses four challenges which are addressed in the following sections. (1) some CVs within the SDSS footprint would have been too bright or too faint to be observed by SDSS; (2) an appropriate value of h for each CV sub-type needs to be chosen; (3) SDSS was not complete and did not target a proportion of CVs within its footprint; (4) the SDSS footprint only achieved partial sky coverage and a method of extrapolating the results derived from the SDSS observations is needed.

6.4.1 CV brightness

SDSS I to IV spectroscopy did not target any objects with $g \lesssim 15$, which has been taken into account in section 6.4.3 below. At the faint end it will be apparent from the HR diagram (Fig. 34) that some sub-types have a larger intrinsic luminosity than others and will therefore be observable at greater distances by SDSS. We therefore sought to establish for each sub-type a limiting distance (R_{lim}) within which they would have reliably been detected by SDSS. To derive this we first assume that CVs with $g < 21$ will be reliably detected from inspection of their SDSS spectrum if targeted; this is a conservative assumption as for example Pâris et al. (2017) used $g < 22$. In the following, we decided to use the *Gaia* G -band magnitude rather than SDSS- g , as the multiple observations of *Gaia* more adequately sample the average brightness of an individual system. The two passbands yield very similar apparent magnitudes for a given brightness. We calculated the mean (μ) and standard deviation (σ) of the absolute *Gaia* G magnitude of each sub-type from the SDSS I to IV CVs (ignoring objects where the error in the Bailer-Jones et al. (2018) distance was greater than 20 per cent). By definition for any CV of a given sub-type with apparent magnitude m , absolute magnitude M and distance d pc there is a 99.7 per cent probability that $M < \mu + 3\sigma$ hence

$$m - 5 \log_{10}(d) + 5 < \mu + 3\sigma \quad (4)$$

$$m < \mu + 3\sigma + 5 \log_{10}(d) - 5 \quad (5)$$

Now $d < R_{\text{lim}}$ is the largest value of d corresponding to $m = 21$:

$$21 = \mu + 3\sigma + 5 \log_{10}(R_{\text{lim}}) - 5 \quad (6)$$

$$5 \log_{10}(R_{\text{lim}}) = 5 + 21 - \mu - 3\sigma \quad (7)$$

$$R_{\text{lim}} = 10^{1+0.2(21-\mu-3\sigma)} \quad (8)$$

The values of R_{lim} for each sub-type are shown in Table 3.

Table 3. Absolute magnitudes and limiting distances of CV sub-types from SDSS I to IV. N is the number of SDSS I to IV objects with reliable distances (see text). μ , σ are the mean and standard deviation of the absolute *Gaia* G magnitudes.

Type	N	μ	σ	R_{lim} (pc)
U Gem	16	7.83	1.13	899
SU UMa	66	9.90	0.94	451
WZ Sge	33	11.77	0.39	412
Polar	39	10.33	1.21	256
Intermediate Polar	7	8.59	1.02	739
Novalike variable	17	5.77	1.03	2676

6.4.2 Scale heights of the different CV sub-types

As we shall see the choice of scale height in the model has a significant effect upon the final estimates of the space density. [Patterson \(1984\)](#) used a single scale height of 150 pc for all sub-types in their analysis as did [Duerbeck \(1984\)](#) (who used 125 ± 22 pc). [Preto-rius et al. \(2007a\)](#) assumed scale heights of 120, 260 and 450 pc (hereafter the P2007 model) for long- P_{orb} systems ($P_{\text{orb}} > 3$ h), normal short- P_{orb} systems ($P_{\text{orb}} < 3$ h) and period bouncers respectively. This was based on the assumption that these systems had increasing ages and therefore, as a result of scattering with other stars, increased space velocities resulting in higher average heights above the Galactic plane ([Kolb & Stehle 1996](#)). We have used the assumptions of P2007 in our work. Where systems do not have an observed period we assign them to one of the three scale heights in P2007 based on their sub-type. U Gem CVs, novalike variables and intermediate polars are assumed to be long-period CVs, short-period systems include SU UMa CVs, polars and WZ Sge CVs with the third category reserved for period bouncers. We attempted to analyse the SDSS I to IV data in order to support the scale height assumptions in P2007 but in practice our samples were not complete to a sufficient Galactic height.

6.4.3 Completeness

SDSS I to IV used complex targeting rules focusing largely on quasars and not CVs (e.g. [Richards et al. 2002](#); [Ross et al. 2012](#); [Dwelly et al. 2017](#)). Fortunately CVs have similar colours to quasars and a significant proportion of quasar candidates were observed by SDSS. However, given that CV sub-types occupy different regions of the *Gaia* HR diagram (and in the colour-colour diagrams used by SDSS for their target selection) the proportion of each sub-type observed by SDSS is not the same. Whilst in principle an analysis could estimate the degree of completeness for each sub-type, such an endeavour would be very complex. We have adopted an empirical approach by analysing version 7.24 of the R&K CV catalogue which contains 1429 CVs. We removed the 117 CVs in the R&K catalogue that were originally discovered by SDSS leaving 1312 systems. The apparent magnitude (“mag1”) of these CVs in their normal state was processed and systems that were too bright ($m < 15$) or too faint ($m > 21$) were also removed³. From this we established that 208 CVs fell within the footprint of SDSS. We then established that 97 of these (46.6 per cent) were re-discovered by SDSS and we assumed that this proportion applies to all CVs and sub-types within

³ Ideally, this analysis would have been done by sub-type but we discovered that the “type1” and “type2” fields in the R&K catalogue were unreliable; in particular many WZ Sge had been classified as SU UMa

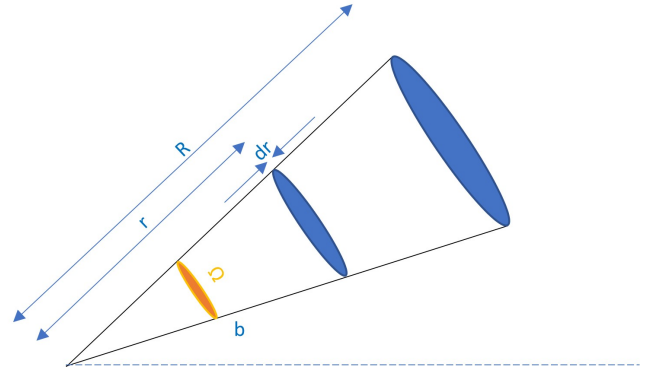


Figure 37. Diagram depicting a slice of infinitesimal thickness dr through a cone subtending a solid angle (Ω) at a radial distance (r). The cone represents one HEALPix pixel. The volume of the slice is $r^2\Omega dr$.

the footprint. We then defined a correction factor $C_{\text{orr}} = 2.14$ as the reciprocal of this proportion.

[Pala et al. \(2020\)](#) used a different approach by quantifying the number of *Gaia* objects within the SDSS footprint which fulfilled the quasar colour criteria for SDSS I and II and did not include any cut in the red colours. This resulted in 5300 objects and [Pala et al. 2020](#) then found the proportion of these objects with an SDSS spectrum (53 per cent) of which ≈ 6 were predicted to be in the sample. Only four were found (three had a spectrum) from which they concluded that the completeness was 71 per cent (i.e. $C_{\text{orr}} = 1.4$). It is unsurprising that the completeness of the full SDSS I to IV sample is lower than that of the nearby, bright 150 pc sample.

6.4.4 SDSS Footprint

The coordinates of the centres of the plates used in the “BOSS”, “eBOSS” and “SDSS” surveys, together with their radius (1.49 degrees), define the coverage. However there are two problems to address; firstly the plates overlap and secondly CVs are not uniformly distributed in space but concentrated near the Galactic plane.

For convenience we define from the denominator of (3) an effective volume for a sphere radius R :

$$V_{\text{eff}}(h, R) = \int_{V(R)} \exp\left(-\frac{|z|}{h}\right) dv \quad (9)$$

To address the overlap problem we model the celestial sphere using 2^8 ASTROPY HEALPix pixels ([Górski et al. 2005](#)). Each HEALPix pixel has the same surface area (Ω steradians) on the unit sphere and can be represented by a cone (Fig. 37). The effective volume of a sphere radius R is therefore the sum of the volume of the cones:

$$V_{\text{eff}}(h, R) = \sum_{\text{All pixels}} \int_0^R \exp\left(-\frac{|r \sin(b)|}{h}\right) (r^2 \Omega dr) \quad (10)$$

The following substitutions are used:

$$A = \frac{|R \sin(b)|}{h} \quad (11)$$

and

$$x = \left(\frac{rA}{R}\right) \quad (12)$$

We then compared the coordinates (ra,dec) of each HealPix pixel with the coordinates of the centre of each plate to identify whether that pixel was covered by that plate. We then defined SDSS_{pix} as the

de-duplicated set of HEALPix pixels that lay within the coverage of one or more plates. The effective volume of the SDSS sample is therefore:

$$\begin{aligned} V_{\text{eff}}(h, R) &= \sum_{\text{SDSS}_{\text{pix}}} \int_0^A \exp(-x) \left(\left(\frac{Rx}{A} \right)^2 \Omega \left(\frac{Rdx}{A} \right) \right) \\ &= \Omega R^3 \sum_{\text{SDSS}_{\text{pix}}} \left(\frac{1}{A^3} \right) \int_0^A x^2 \exp(-x) dx \end{aligned} \quad (13)$$

Solving the integral analytically yields

$$V_{\text{eff}}(h, R) = \Omega R^3 \sum_{\text{SDSS}_{\text{pix}}} \left(\frac{1}{A^3} \right) \left(2 - (A^2 + 2A + 2) \exp(-A) \right) \quad (14)$$

which can be computed numerically for a given h and R .

6.4.5 Estimates of space density

Bringing the preceding sections together the three estimates of the space density (for $h = 120, 260, 450$ pc) are calculated from

$$\rho_0 = \frac{N_{\text{obs}} \times C_{\text{orr}}}{V_{\text{eff}}(h, R_{\text{lim}})} \quad (15)$$

and the results are listed in Table 4.

Next, we need to discuss the accuracy of these results. From equation (15) the primary sources of error in ρ_0 are in the correction factor and the scale height. The true scale height in each case will very likely lie between the two extreme values that we adopted, i.e. $h = 120$ pc and $h = 450$ pc (Table 4) and so a reasonable estimate for ρ_0 (excepting possibly old WZ Sge systems) is $\rho_0(260$ pc) with the extreme values forming a notional 3σ error estimate. We have avoided quoting any statistical uncertainties on our space density estimates as the true uncertainties are likely to be dominated by the assumptions on the scale height.

It is interesting to compare these estimates with the those based on different approaches used in previous works (Fig. 38) noting that the assumed scale heights have to be comparable.

Section 9.5 in Warner (1995) proposed $\rho_0(103$ pc) = $0.4 \times 10^{-6} \text{ pc}^{-3}$ for U Gem type systems and $\rho_0(176$ pc) = $0.25 \times 10^{-6} \text{ pc}^{-3}$ for SU UMa systems. Both values are lower than contemporary estimates presumably as earlier CV discoveries were primarily the result of following up transients and limited to brighter targets.

Pretorius et al. (2007b) estimated $\rho_0(120$ pc) = $(15^{+25}_{-8}) \times 10^{-6} \text{ pc}^{-3}$ for all non-magnetic CVs based on a very small sample of four systems. Our results are towards the lower end of this range.

Pretorius & Knigge (2012) estimated a density of $\rho_0(260$ pc) = $(3.8^{+5.3}_{-1.9}) \times 10^{-6} \text{ pc}^{-3}$ for non-magnetic CVs which compares with our value of $\rho_0(260$ pc) = $(4.29) \times 10^{-6} \text{ pc}^{-3}$ (by adding the individual estimates from Table 4).

Pretorius et al. (2013) estimated $\rho_0 = (1.3^{+0.6}_{-0.4}) \times 10^{-6} \text{ pc}^{-3}$ for magnetic CVs, based upon a scale height of 120 pc for long period systems and 260 pc for short period systems, which is consistent with our estimates. They also estimated values for polars and intermediate polars which are consistent with this work.

Schwope (2018) estimated $\rho_0(120$ pc) = $0.13 \times 10^{-6} \text{ pc}^{-3}$ for intermediate polars. This is significantly lower than our estimate.

Pala et al. (2020) estimated a composite $\rho_0(280$ pc) = $(4.8^{+0.6}_{-0.8}) \times 10^{-6} \text{ pc}^{-3}$ for all CVs and our $\rho_0(260$ pc) = $5.78 \times$

10^{-6} pc^{-3} is consistent with this noting that we use a larger correction factor (2.1 compared with 1.4 in Pala et al. (2020)). Pala et al. (2020) also provided incomplete (their footnote 9 states that they were unable to estimate the completeness of individual sub-types) estimates for $\rho_0(260$ pc) for five sub-types. These values are lower than our estimates – partly due to (in)completeness but also because we use a larger correction factor (2.1 compared with 1.4 in Pala et al. (2020)). Our larger sample size may also have had an effect brought about by the effectiveness of SDSS in discovering short-period systems.

Inight et al. 2021 estimated $\rho_0 = (2.23^{+1.04}_{-0.6}) \times 10^{-6} \text{ pc}^{-3}$ for their Gold Sample of 201 systems. The Gold Sample is a reliable subset of the known CVs (at least 305) within 300 pc and their estimate is therefore a lower limit for the true space density.

In principle, the fractions of sub-types from our space density estimates should reflect the true fractions in the underlying population without selection effects – as opposed to the number ratios in the magnitude limited SDSS I to IV sample. We therefore compared these fractions with those from the SDSS I to IV sample (Fig. 39), where the main difference is the larger proportion of WZ Sge stars and a lower fraction of SU UMa CVs when looking at the space density results. This is in line with the expectation that low-luminosity WZ Sge stars should be under-represented in a magnitude limited sample. Whilst demonstrating that the SDSS I to IV sample is subject to some selection effects, we also caution not to over-interpret the space density ratios because of the significant effect of scale height assumptions.

In summary, the long-standing discussion of the CV space density seems to converge to a value of $\approx 5 \times 10^{-6} \text{ pc}^{-3}$. However, the uncertainties in scale heights continue to limit the accuracy of any estimates of space density. We have calculated space densities for six sub-types and Fig. 38 demonstrates that these estimates are consistent with other work.

6.5 Low accretion rate systems

Period bouncers are CVs where the mass of the donor has shrunk below the level needed to sustain hydrogen fusion in the core ($\approx 0.061 M_{\odot}$) and the donor has evolved to a brown dwarf. A consequence of this is that the orbital separation of the CV increases and P_{orb} evolves back from the period minimum (often taken as ~ 76.2 min, Knigge 2006) towards longer periods. Patterson (2011) identified a total of 22 candidate period bouncers, eight of which are in our sample (Table 5). Together with one polar, the 13 non-magnetic period-bouncers in Table 5 represent 14 per cent of the WZ Sge CVs and 2.6 per cent of our complete sample. The two new candidates from this work (J0904+4402 and J2131–0039) were identified because of their spectra (white dwarf visible and donor not apparent) and an orbital period significantly larger than the period minimum. We estimated the space density of period bouncers using 14 per cent of the space density of WZ Sge from Table 4 to be $\rho_0(450) = 0.27 \times 10^{-6} \text{ pc}^{-3}$. Comparing this with $\rho_0(P2007) = 7.92 \times 10^{-6} \text{ pc}^{-3}$ implies that only 3.4 per cent of CVs are period bouncers which is a long way from the 70 per cent of all CVs predicted by Kolb (1993). Goliasch & Nelson (2015) modelled CV evolution to predict the intrinsic proportion of period bouncers as being 38 – 60 per cent of all CVs and the observed proportion (taking account of selection effects) as 2.5 – 11.2 per cent. Although period bouncers are intrinsically faint any observational bias is unlikely to fully account for this difference. As long as period bouncers maintain a minimum amount of mass transfer, and associated Balmer emission lines, SDSS spectroscopy is extremely

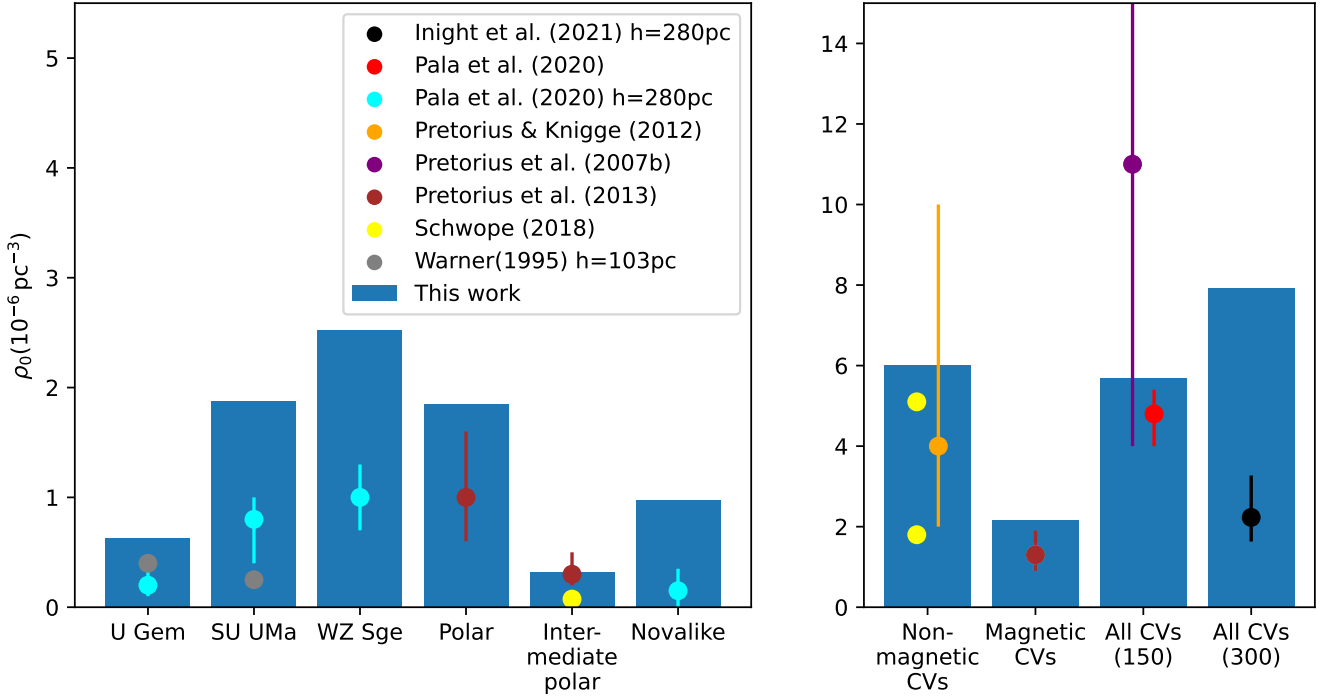


Figure 38. Comparison of the space density estimates for CVs from this work (bar chart) and published values. All estimates use the P2007 assumptions for scale height h unless otherwise stated. Left panel: Estimates for individual sub-types. Note that Pala et al. (2020) are understated as they do not take account of completeness. Right panel: Composite estimates. Inight et al. (2021) specifically excluded selection effects.

Table 4. Analysis of the space density of CV sub-types for different assumptions of scale height. ρ_0 (P2007) assumes the scale heights from Pretorius et al. (2007a). N is the number of SDSS I to IV objects that are closer than the limiting distance. Note that the values of ρ_0 for individual sub-types are slightly understated (≈ 6 per cent) due to the remaining unclassified CVs and dwarf novae. This does not apply to the “All CVs” values which have been calculated for 150 pc and 300 pc limiting distances to enable comparison with Pala et al. (2020) and Inight et al. (2021) respectively.

Type	Limiting distance (pc)	N	Space Density (10^{-6}pc^{-3})			
			$\rho_0(120)$	$\rho_0(260)$	$\rho_0(450)$	$\rho_0(P2007)$
U Gem	899	10	0.68	0.16	0.09	0.63
SU UMa	451	30	4.21	1.71	1.19	1.88
WZ Sge	412	38	6.24	2.72	1.96	2.52
Polar	256	8	3.25	1.89	1.53	1.84
Intermediate polar	739	6	0.50	0.14	0.08	0.32
Novalike	2676	23	1.01	0.12	0.04	0.97
All CVs	150	7	8.21	5.78	5.07	5.68
All CVs	300	52	13.92	7.23	5.61	7.92

efficient at identifying WZ Sge CVs, independent of their orbital period and their outburst frequency. The lack of observed period bouncers remains puzzling, and could be due to the donors in period bouncers either becoming detached or merging with the white dwarfs.

6.6 Unusual state changes

In contrast to dwarf novae, which undergo quasi-regular outbursts because of thermal instabilities in their accretion discs, novalike variables are known to exhibit state changes due to sustained changes in \dot{M} (Shafter et al. 1985; Leach et al. 1999; Rodríguez-Gil et al. 2007). Polars are also known to undergo state changes on a timescale of months to years (Kafka & Honeycutt 2005; Ramsay et al. 2004;

Šimon 2016), and low states have been observed occasionally in a small number of dwarf novae (Wood et al. 1995; Schreiber et al. 2002). The cause of the high/low state transitions is still debated, but a likely contender is star spots near the inner Lagrangian point (Livio & Pringle 1994; King & Cannizzo 1998; Hessman et al. 2000)

Serendipitously whilst reviewing the ZTF light curves of the spectroscopically identified CVs we have identified eight CVs (Figure. 40) within the SDSS I to IV sample that display erratic light curve morphologies, neither displaying disc outbursts, nor clearly identifiable state changes – and which have spectra that are inconsistent with being either magnetic CVs or novalike variables. These systems defy the standard CV classification scheme outlined in section 3. These eight examples of systems exhibit significant

Table 5. Period bouncers within the coverage of SDSS I to IV. Candidate systems are shown in italics. The mass ratio of two systems were identified using the method from [Kato & Osaki \(2013\)](#); the donor mass is estimated by assuming a maximum white dwarf mass of $1.4M_{\odot}$ and is therefore definitely low enough to form a brown dwarf. J1212+0136 is an interesting system as it was initially assumed to be a detached system with a white dwarf and low mass companion. It was only recognised as an accreting system from the detection of cyclotron emissions and an X-ray observation which also confirmed its type.

SDSS name	CV type	Reference	P_{orb} (h)	$M_{\text{donor}} (M_{\odot})$
<i>J0058-0107</i>	WZ Sge	Kato et al. (2017)	1.559	q=0.079
J0804+5103	WZ Sge	Amantayeva et al. (2021)	1.433	0.042
J0843+2751	WZ Sge	Patterson et al. (1998)	1.439	0.02
<i>J0904+4402</i>	WZ Sge:	This work	1.674	
J1035+0551	WZ Sge:	Littlefair et al. (2006)	1.368	0.06
J1057+2759	WZ Sge:	McAllister et al. (2017)	1.507	0.044
<i>J1212+0136</i>	Polar	Farihi et al. (2008)	1.474	
J1216+0520	WZ Sge:	Southworth et al. (2006)	1.646	<.04
J1255+2642	WZ Sge	Patterson et al. (2005a)	1.992	<.05
J1433+1011	WZ Sge	Savoury et al. (2011)	1.302	0.0571
J1435+2336	WZ Sge:	Pala et al. (2022)	1.296	
J1507+5230	WZ Sge	Littlefair et al. (2007)	1.11	0.056
<i>J2131-0039</i>	WZ Sge:	This work	1.67	
J2304+0625	WZ Sge	Nakata et al. (2014)	1.616	q=.053

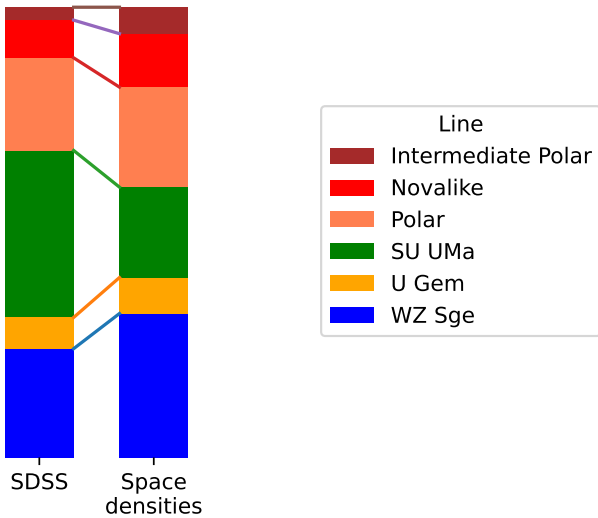


Figure 39. Comparison of the distribution of sub-types between the SDSS I to IV sample and our predicted space densities using the P2007 scale height assumptions. This plot ignores sub-types for which we have not estimated a space density.

brightness changes on timescales that indicate the cause is a change to \dot{M} rather than instabilities of their discs. Below, we discuss the properties of these systems.

J0838+4910 is below the period gap with $P_{\text{orb}} = 1.69$ h. [Thorstensen et al. \(2015\)](#) rightly concluded that this was an SU UMa based on the measured orbital period and the CRTS light curve. The SDSS spectrum is consistent with an SU UMa classification. However the ZTF data is contradictory – showing no outbursts and two long-lasting faint states.

J0853+4848 has a spectrum that shows Balmer, He I and weak He II emission lines. The white dwarf is not visible but the M-type donor is detected in the red part of the spectrum. The system has been brighter since the SDSS spectrum was obtained. There is no CRTS data and the ZTF data shows one small outburst but also state changes of up to two magnitudes. The period is 2.36 h which is in the period gap.

J0922+3103 (AR Cnc) and J1544+2553 have periods of 5.15 h and 6.03 h respectively and spectra which resemble U Gem CVs with double-peaked Balmer and helium lines, and clear signatures of their M-dwarf donors. However their light curves more closely resemble those of polars and they exhibit no outbursts. This ambiguity prevents any further classification beyond that of a CV. [Palaversa et al. \(2013\)](#) classified J1544+2553 as a novalike using an automated process but this is not consistent with the strong lines in the spectrum, the detection of the donor and the position in the HR diagram.

J1239+2108 (IR Com) has previously been identified as a CV with erratic brightness changes ([Richter et al. 1997](#)), and SDSS obtained a spectrum when accretion had virtually ceased for an extended period ([Manser & Gansicke 2014](#)), revealing both the white dwarf and the donor star. It is on the lower edge of the period gap with $P_{\text{orb}} = 2.09$ h.

J1244+3004 (CSS 080427:124418+300401) was found in a bright state within the CRTS light curve for about ten years, albeit exhibiting outbursts ([Thorstensen et al. 2015](#)). The ZTF light curve (Fig. 40) shows a prolonged drop of $m \simeq 2$. Its period of $P_{\text{orb}} = 1.86$ h places it below the period gap.

J2309+2135 (V405 Peg) was identified by [Schwope et al. \(2002b\)](#) as the counterpart of a *ROSAT* X-ray source, and based on the detection of the donor star, and the apparent magnitude, the authors speculated that V405 Peg may be as close as $\simeq 30$ pc. [Thorstensen et al. \(2009\)](#) determined the period to be 4.26 h, and measured a parallax of $\simeq 150$ pc – superseded by the *Gaia* parallax of $\simeq 173$ pc. [Schwope et al. \(2014\)](#) obtained deep X-ray observations, revealing a relatively low X-ray luminosity, and the authors noted that the system displays characteristics of both magnetic and non-magnetic CVs. The SDSS spectrum very clearly reveals the M-type donor star, with little contribution from either an accretion disc or the white dwarf.

J2330+3033 has a spectrum showing both Balmer and He I emission lines, the donor is clearly visible. It is eclipsing and [Hardy et al. \(2017\)](#) found $P_{\text{orb}} = 3.74$ h. The CRTS and ZTF light curves show variability but no outbursts.

We note that the periods of these systems cluster both near the lower edge of the period gap, and in the $\simeq 4 - 6$ h range, indicating widely varying evolutionary stages. The lack of outbursts is indica-

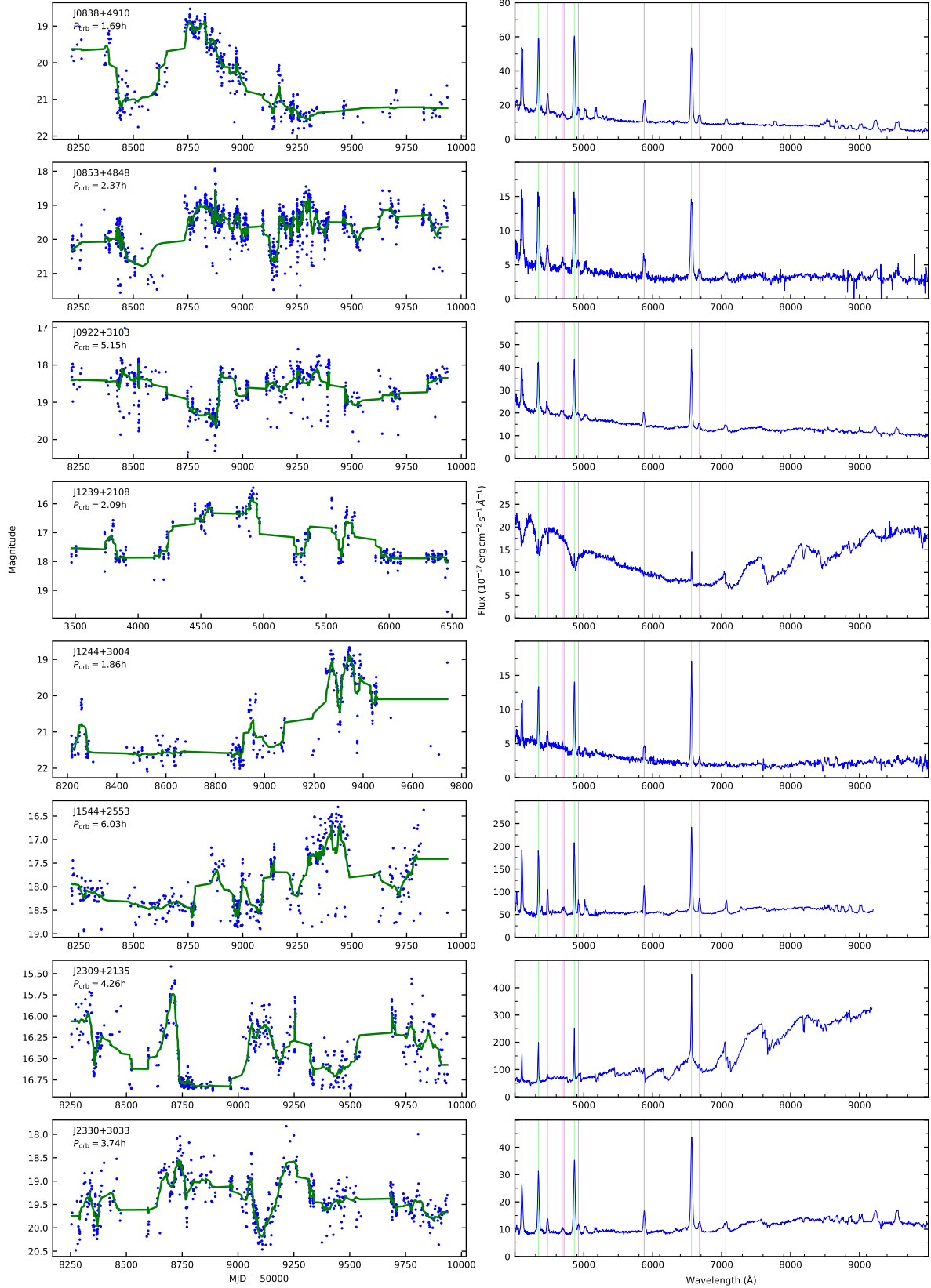


Figure 40. We identified eight CVs with substantial and erratic changes in apparent magnitude over periods of months or years – suggesting commensurate changes in accretion rate. The light curves shown are the merged r - and g -band data from ZTF, with the exception of J1239+2108 for which we show the CRTS data. The green lines show the trend using five point boxcar smoothing. The changes are atypical as the spectra of these systems are inconsistent with either a magnetic CV or novalike variable classification.

tive of a low \dot{M} . A low \dot{M} is corroborated by the detection of the donor stars in the short-period systems, as non-magnetic CVs within this period range are typically SU UMa systems with accretion disc dominated spectra. The long-period systems coincide with the period range where dwarf novae are usually found (we encourage the reader to inspect section 7.2 of [Knigge et al. 2011](#) for a discussion of the inconsistency between the CV sub-type distribution in the 3 – 6 h period range and the theoretical predictions of \dot{M} and the critical accretion rate for disc instabilities to (not) occur). We speculate that these eight systems may either contain weakly magnetic white dwarfs, with fields that are sufficiently low so that they do not develop the hallmarks of polars or intermediate polars, but strong enough to affect the structure of the disc. However, we also note that a number of intermediate polars exhibit dwarf nova outbursts – so the tentative suggestion of weak fields does not explain the absence of outbursts. An alternative idea is that these systems are undergoing some type of state change in their donor stars, as possibly suggested by their location near the lower edge of the period gap, and in the range where dwarf novae and novalike overlap above the period gap.

6.7 Tertiary systems

[Raghavan et al. \(2010\)](#) suggest that around eight per cent of close binaries are part of a triple system and have a distant companion. They are significant as the distant star can influence the evolution of the inner binary through Kozai cycles ([Fabrycky & Tremaine 2007](#)). We searched *Gaia* EDR3 for such systems by identifying candidate stars within 30 arcsec of each of the CVs in our sample. Potential companions can be expected to have similar proper motions. However proper motions, and hence differences between them, will scale inversely with distance. We therefore adopted the following metric where the denominator is a proxy for distance:

$$\sqrt{\frac{(\text{pmra}_{\text{cv}} - \text{pmra}_{\text{cand}})^2 + (\text{pmdec}_{\text{cv}} - \text{pmdec}_{\text{cand}})^2}{\text{pmra}_{\text{cv}}^2 + \text{pmdec}_{\text{cv}}^2}} < 0.05 \quad (16)$$

resulting in the eight systems in Table 6.

The projected separations, a , were calculated by multiplying the angular separation by the [Bailer-Jones et al. \(2018\)](#) distance; the errors on the [Bailer-Jones et al. \(2018\)](#) distances are too large to estimate the radial separation. Estimating the binding energy is a useful test of whether these systems are gravitationally bound to the CV or not:

$$-E_{\text{bind}} = G \frac{(M_{\text{WD}} + M_{\text{d}})M_3}{a} \quad (17)$$

A rough estimate is sufficient for this purpose and so we assume typical values of $M_{\text{WD}} = 0.83 M_{\odot}$ and a donor of mass $M_{\text{d}} = 0.14 M_{\odot}$. We estimate M_3 from the position of the star in the *Gaia* HR diagram; and find that the CV companion in seven of the tertiaries is on the main sequence; the companion to J1206+5100 is a white dwarf. The calculated values shown in Table 6, when compared with fig 6b of [Burgasser et al. \(2007\)](#) show clearly that these eight CVs are tertiary systems. These eight are only 1.6 per cent of our sample and should be considered a lower limit on the fraction of CVs in triple systems. Our search is likely to be incomplete at larger distances where *Gaia* may not resolve close tertiaries or not detect them because they are too faint; in particular tertiaries with very low-mass or cool white dwarf companions would be hard to identify.

7 SUMMARY

We have reviewed the spectra of CVs observed by SDSS I to IV and publish 178 for the first time along with 59 new periods. We discovered 70 completely new CVs and classified or updated 262. These 70 new CVs from SDSS III and IV augment the 282 previously identified in SDSS I and II. This total is remarkably consistent with the early prediction of 400 from [Szkody et al. \(2002\)](#). We have analysed the results and position the different CV sub-types in evolutionary terms together with revised estimates of space density. The period bouncers and tertiary systems within our sample have been identified and the abundances compared with previous estimates.

ACKNOWLEDGEMENTS

We thank the anonymous referee for their helpful comments.

We acknowledge with thanks the variable star observations from the AAVSO International Database contributed by observers worldwide and used in this research.

Funding for SDSS-III has been provided by the Alfred P. Sloan Foundation, the Participating Institutions, the National Science Foundation, and the U.S. Department of Energy Office of Science. The SDSS-III web site is <http://www.sdss3.org/>.

SDSS-III is managed by the Astrophysical Research Consortium for the Participating Institutions of the SDSS-III Collaboration including the University of Arizona, the Brazilian Participation Group, Brookhaven National Laboratory, Carnegie Mellon University, University of Florida, the French Participation Group, the German Participation Group, Harvard University, the Instituto de Astrofísica de Canarias, the Michigan State/Notre Dame/JINA Participation Group, Johns Hopkins University, Lawrence Berkeley National Laboratory, Max Planck Institute for Astrophysics, Max Planck Institute for Extraterrestrial Physics, New Mexico State University, New York University, Ohio State University, Pennsylvania State University, University of Portsmouth, Princeton University, the Spanish Participation Group, University of Tokyo, University of Utah, Vanderbilt University, University of Virginia, University of Washington, and Yale University.

Funding for the Sloan Digital Sky Survey IV has been provided by the Alfred P. Sloan Foundation, the U.S. Department of Energy Office of Science, and the Participating Institutions. SDSS acknowledges support and resources from the Center for High-Performance Computing at the University of Utah. The SDSS web site is www.sdss.org.

SDSS IV is managed by the Astrophysical Research Consortium for the Participating Institutions of the SDSS Collaboration including the Brazilian Participation Group, the Carnegie Institution for Science, Carnegie Mellon University, Center for Astrophysics | Harvard & Smithsonian (CfA), the Chilean Participation Group, the French Participation Group, Instituto de Astrofísica de Canarias, The Johns Hopkins University, Kavli Institute for the Physics and Mathematics of the Universe (IPMU) / University of Tokyo, the Korean Participation Group, Lawrence Berkeley National Laboratory, Leibniz Institut für Astrophysik Potsdam (AIP), Max-Planck-Institut für Astronomie (MPIA Heidelberg), Max-Planck-Institut für Astrophysik (MPA Garching), Max-Planck-Institut für Extraterrestrische Physik (MPE), National Astronomical Observatories of China, New Mexico State University, New York University, University of Notre Dame, Observatório Nacional / MCTI, The Ohio State University, Pennsylvania State University, Shanghai Astronomical Observatory, United Kingdom Participation Group, Universidad Nacional Autónoma de México, University of Arizona,

Table 6. Tertiary systems identified in SDSS I to IV. μ_{RA} and μ_{Dec} are the components of proper motion and a is the projected separation. In each case the calculated binding energy $-E_{bind}$ (see text for details) is typical of a bound system as shown in fig. 6b of Burgasser et al. (2007).

System	<i>Gaia</i> EDR3 source_id	P_{orb} (h)	Distance (pc)	μ_{RA} (mas yr $^{-1}$)	μ_{Dec} (mas yr $^{-1}$)	a (au)	$-E_{bind}$ (10 41 erg)
J0801+2103	670872860843747072		816 ± 106	-9.22	-17.26	12682 ± 2720	7 ± 1.6
	670872860843744768		1597 ± 608	-8.97	-17.20		
J0803+2516	681813727390427136	2.2	1016 ± 130	-7.63	-7.52	4922 ± 976	22 ± 4.3
	681813723094550144		1042 ± 72	-7.80	-7.22		
J0840+0455	582480170443653376		1466 ± 104	-3.92	-11.11	862 ± 106	142 ± 17.5
	582480166148927744		1441 ± 120	-3.88	-11.00		
J1014+0638	3873721404734233344	1.4	192 ± 5	-62.27	-34.29	1680 ± 80	56 ± 2.7
	3873721409029428352		185 ± 1	-62.89	-34.03		
J1131+4322	772038105376131456	1.5	328 ± 6	-12.78	11.70	1745 ± 65	54 ± 2.0
	772038105376626432		361 ± 5	-12.66	11.94		
J1206+5100	1548430890981046272	3.8	302 ± 8	0.46	-28.23	2080 ± 112	39 ± 2.1
	1548430886684193152		317 ± 49	-0.48	-28.00		
J1702+2235	4571234234022916992	1.6	3237 ± 1269	4.42	-6.84	1447 ± 847	63 ± 36.9
	4571234234022916864		1605 ± 1238	4.40	-6.74		
J2205+1155	2728239161441977216	1.4	1004 ± 451	15.91	-9.58	18470 ± 11519	5 ± 2.9
	2728239200096378368		544 ± 42	16.67	-9.42		

University of Colorado Boulder, University of Oxford, University of Portsmouth, University of Utah, University of Virginia, University of Washington, University of Wisconsin, Vanderbilt University, and Yale University.

Based on observations obtained with the Samuel Oschin Telescope 48-inch and the 60-inch Telescope at the Palomar Observatory as part of the Zwicky Transient Facility project. ZTF is supported by the National Science Foundation under Grants No. AST-1440341 and AST-2034437 and a collaboration including current partners Caltech, IPAC, the Weizmann Institute for Science, the Oskar Klein Center at Stockholm University, the University of Maryland, Deutsches Elektronen-Synchrotron and Humboldt University, the TANGO Consortium of Taiwan, the University of Wisconsin at Milwaukee, Trinity College Dublin, Lawrence Livermore National Laboratories, IN2P3, University of Warwick, Ruhr University Bochum, Northwestern University and former partners the University of Washington, Los Alamos National Laboratories, and Lawrence Berkeley National Laboratories. Operations are conducted by COO, IPAC, and UW.

Data from the Catalina Real-Time Transient Survey has been used (Drake et al. 2009)

This work has made use of data from the European Space Agency (ESA) mission *Gaia* (<https://www.cosmos.esa.int/gaia>), processed by the *Gaia* Data Processing and Analysis Consortium (DPAC, <https://www.cosmos.esa.int/web/gaia/dpac/consortium>). Funding for the DPAC has been provided by national institutions, in particular the institutions participating in the *Gaia* Multilateral Agreement.

This paper includes data collected with the TESS mission, obtained from the MAST data archive at the Space Telescope Science Institute (STScI). Funding for the TESS mission is provided by the NASA Explorer Program. STScI is operated by the Association of Universities for Research in Astronomy, Inc., under NASA contract NAS 5–26555.

This work makes use of observations obtained at the MDM

Observatory, operated by Dartmouth College, Columbia University, Ohio State University, Ohio University, and the University of Michigan.

Guoshoujing Telescope (the Large Sky Area Multi-Object Fiber Spectroscopic Telescope LAMOST) is a National Major Scientific Project built by the Chinese Academy of Sciences. Funding for the project has been provided by the National Development and Reform Commission. LAMOST is operated and managed by the National Astronomical Observatories, Chinese Academy of Sciences.

Some of the results in this paper have been derived using the healpy and HEALPix package.

BTG was supported by grant ST/T000406/1 from the Science and Technology Facilities Council (STFC). This project has received funding from the European Research Council (ERC) under the European Union’s Horizon 2020 research and innovation programme (Grant agreement No. 101020057). This research was supported in part by the National Science Foundation under Grant No. PHY-1748958.

DATA AVAILABILITY

All data used in this article are available from the sources referenced in the text. The Supplementary Data including a machine-readable version of the catalogue is included in the online version of this paper.

REFERENCES

- Abazajian K., et al., 2003, *AJ*, **126**, 2081
 Abazajian K. N., et al., 2009, *ApJS*, **182**, 543
 Abril J., Schmidtbreick L., Ederoclite A., López-Sanjuan C., 2020, *MNRAS*, **492**, L40
 Adelman-McCarthy J. K., et al., 2008, *ApJS*, **175**, 297
 Aguado D. S., et al., 2019, *ApJS*, **240**, 23
 Aihara H., et al., 2011, *ApJS*, **193**, 29

- King A. R., Cannizzo J. K., 1998, *ApJ*, **499**, 348
- Kleinman S. J., et al., 2013, *ApJS*, **204**, 5
- Knigge C., 2006, *MNRAS*, **373**, 484
- Knigge C., Baraffe I., Patterson J., 2011, *ApJS*, **194**, 28
- Kochukhov O., 2021, *A&ARv*, **29**, 1
- Kolb U., 1993, *A&A*, **271**, 149
- Kolb U., Baraffe I., 1999, *MNRAS*, **309**, 1034
- Kolb U., Stehle R., 1996, *MNRAS*, **282**, 1454
- Kraft R. P., 1963, *Advances in Astronomy and Astrophysics*, **2**, 43
- Leach R., Hessman F. V., King A. R., Stehle R., Mattei J., 1999, *MNRAS*, **305**, 225
- Liaw A., Wiener M., 2001, *Forest*, 23
- Lightkurve Collaboration et al., 2018, Lightkurve: Kepler and TESS time series analysis in Python, Astrophysics Source Code Library, record ascl:1812.013 (ascl:1812.013)
- Lindgren L., 2018, Re-normalising the astrometric chi-square in Gaia DR2, GAIA-C3-TN-LU-LL-124, http://www.rssd.esa.int/doc_fetch.php?id=3757412
- Lindgren L., et al., 2018, *A&A*, **616**, A2
- Littlefair S. P., Dhillon V. S., Marsh T. R., Gänsicke B. T., Southworth J., Watson C. A., 2006, *Science*, **314**, 1578
- Littlefair S. P., Dhillon V. S., Marsh T. R., Gänsicke B. T., Baraffe I., Watson C. A., 2007, *MNRAS*, **381**, 827
- Liu W.-M., Jiang L., Chen W.-C., 2021, *ApJ*, **910**, 22
- Livio M., Pringle J. E., 1994, *ApJ*, **427**, 956
- Manser C. J., Gänsicke B. T., 2014, *MNRAS*, **442**, L23
- Masci F. J., et al., 2018, *Publications of the Astronomical Society of the Pacific*, **131**, 018003
- Mason P. A., Wells N. K., Motsoaledi M., Szkody P., Gonzalez E., 2019, *MNRAS*, **488**, 2881
- McAllister M. J., et al., 2017, *MNRAS*, **467**, 1024
- Merc J., et al., 2021, *MNRAS*, **506**, 4151
- Meyer F., Meyer-Hofmeister E., 1983, *A&A*, **121**, 29
- Mróz P., et al., 2016, *Nature*, **537**, 649
- Mukadam A. S., Gänsicke B. T., Szkody P., Aungwerojwit A., Howell S. B., Fraser O. J., Silvestri N. M., 2007, *ApJ*, **667**, 433
- Munari U., Mason E., Valisa P., 2014, *A&A*, **564**, A76
- Nakata C., et al., 2014, *PASJ*, **66**, 116
- Nelemans G., Yungelson L. R., Portegies Zwart S. F., 2004, *MNRAS*, **349**, 181
- Nelemans G., Siess L., Repetto S., Toonen S., Phinney E. S., 2016, *ApJ*, **817**, 69
- Norton A. J., Wynn G. A., Somerscales R. V., 2004, *ApJ*, **614**, 349
- Norton A. J., Butters O. W., Parker T. L., Wynn G. A., 2008, *ApJ*, **672**, 524
- Osaki Y., 1989, *PASJ*, **41**, 1005
- Paczynski B., 1967, *Acta Astron.*, **17**, 287
- Paczynski B., 1976, in Eggleton P., Mitton S., Whelan J., eds, *Proceedings of the International Astronomical Union Vol. 73, Structure and Evolution of Close Binary Systems*. p. 75
- Paczynski B., Sienkiewicz R., 1983, *ApJ*, **268**, 825
- Pala A. F., et al., 2017, *MNRAS*, **466**, 2855
- Pala A. F., Schmidtbreick L., Tappert C., Gänsicke B. T., Mehner A., 2018, *MNRAS*, **481**, 2523
- Pala A. F., et al., 2020, *MNRAS*, **494**, 3799
- Pala A. F., et al., 2022, *MNRAS*, **510**, 6110
- Palaversa L., et al., 2013, *AJ*, **146**, 101
- Pâris I., et al., 2017, *A&A*, **597**, A79
- Parsons S. G., et al., 2013, *MNRAS*, **429**, 256
- Parsons S. G., et al., 2015, *MNRAS*, **449**, 2194
- Parsons S. G., Gänsicke B. T., Schreiber M. R., Marsh T. R., Ashley R. P., Breedt E., Littlefair S. P., Meusinger H., 2021, *MNRAS*, **502**, 4305
- Patterson J., 1984, *ApJS*, **54**, 443
- Patterson J., 1994, *PASP*, **106**, 209
- Patterson J., 2011, *MNRAS*, **411**, 2695
- Patterson J., et al., 1998, *PASP*, **110**, 1290
- Patterson J., et al., 2002, *PASP*, **114**, 721
- Patterson J., Thorstensen J. R., Kemp J., 2005a, *PASP*, **117**, 427
- Patterson J., et al., 2005b, *PASP*, **117**, 1204
- Patterson J., et al., 2013, *MNRAS*, **434**, 1902
- Pavlenko E. P., et al., 2018, *MNRAS*, **479**, 341
- Pirola V., Coyne G. V., Takalo S. J., Takalo L., Larsson S., Vilhu O., 1994, *A&A*, **283**, 163
- Podsiadlowski P., Han Z., Rappaport S., 2003, *MNRAS*, **340**, 1214
- Pretorius M. L., Knigge C., 2012, *MNRAS*, **419**, 1442
- Pretorius M. L., Knigge C., Kolb U., 2007a, *MNRAS*, **374**, 1495
- Pretorius M. L., Knigge C., O'Donoghue D., Henry J. P., Gioia I. M., Mullis C. R., 2007b, *MNRAS*, **382**, 1279
- Pretorius M. L., Knigge C., Schwöpe A. D., 2013, *MNRAS*, **432**, 570
- Raghavan D., et al., 2010, *ApJS*, **190**, 1
- Ramsay G., Cropper M., Wu K., Mason K. O., Córdova F. A., Priedhorsky W., 2004, *MNRAS*, **350**, 1373
- Ramsay G., et al., 2018, *A&A*, **620**, A141
- Rappaport S., Verbunt F., Joss P. C., 1983, *ApJ*, **275**, 713
- Rebassa-Mansergas A., Gänsicke B. T., Schreiber M. R., Koester D., Rodríguez-Gil P., 2010, *MNRAS*, **402**, 620
- Rebassa-Mansergas A., Nebot Gómez-Morán A., Schreiber M. R., Gänsicke B. T., Schwöpe A., Gallardo J., Koester D., 2012, *MNRAS*, **419**, 806
- Rebassa-Mansergas A., Parsons S. G., Copperwheat C. M., Justham S., Gänsicke B. T., Schreiber M. R., Marsh T. R., Dhillon V. S., 2014, *ApJ*, **790**, 28
- Rebull L., et al., 2019, in Molinaro M., Shortridge K., Pasian F., eds, *Astronomical Society of the Pacific Conference Series Vol. 521, Astronomical Data Analysis Software and Systems XXVI*. p. 36
- Reimers D., Hagen H. J., Hopp U., 1999, *A&A*, **343**, 157
- Reiners A., Basri G., 2009, *A&A*, **496**, 787
- Richards G. T., et al., 2002, *AJ*, **123**, 2945
- Richter G. A., Kroll P., Greiner J., Wenzel W., Luthardt R., Schwarz R., 1997, *A&A*, **325**, 994
- Ricker G. R., et al., 2015, *Journal of Astronomical Telescopes, Instruments, and Systems*, **1**, 014003
- Ritter H., Kolb U., 1998, *A&AS*, **129**, 83
- Ritter H., Kolb U., 2003, *A&A*, **404**, 301
- Robertson J. W., Honeycutt R. K., Turner G. W., 1995, *PASP*, **107**, 443
- Rodríguez-Gil P., et al., 2005, *A&A*, **440**, 701
- Rodríguez-Gil P., et al., 2007, *MNRAS*, **377**, 1747
- Rodríguez-Gil P., Torres M. A. P., Gänsicke B. T., Muñoz-Darias T., Steeghs D., Schwarz R., Rau A., Hagen H. J., 2009, *A&A*, **496**, 805
- Ross N. P., et al., 2012, *ApJS*, **199**, 3
- Ryu K., et al., 2006, *ApJ*, **644**, L185
- Savouiry C. D. J., et al., 2011, *MNRAS*, **415**, 2025
- Scaringi S., Maccarone T. J., D'Angelo C., Knigge C., Groot P. J., 2017, *Nature*, **552**, 210
- Schimeczek C., Wunner G., 2014, *ApJS*, **212**, 26
- Schmidt G. D., et al., 2005, *ApJ*, **630**, 1037
- Schmidt G. D., Smith P. S., Szkody P., Anderson S. F., 2008, *PASP*, **120**, 160
- Schreiber M. R., Gänsicke B. T., Mattei J. A., 2002, *A&A*, **384**, L6
- Schreiber M. R., Zorotovic M., Wijnen T. P. G., 2016, *MNRAS*, **455**, L16
- Schreiber M. R., Belloni D., Gänsicke B. T., Parsons S. G., Zorotovic M., 2021, *Nature Astronomy*, **5**, 648
- Schwarzenberg-Czerny A., 1996, *ApJ*, **460**, L107
- Schwöpe A. D., 2018, *A&A*, **619**, A62
- Schwöpe A. D., Beuermann K., Jordan S., Thomas H. C., 1993, *A&A*, **278**, 487
- Schwöpe A. D., Brunner H., Hambaryan V., Schwarz R., 2002a, in Gänsicke B. T., Beuermann K., Reinsch K., eds, *Astronomical Society of the Pacific Conference Series Vol. 261, The Physics of Cataclysmic Variables and Related Objects*. p. 102
- Schwöpe A. D., Brunner H., Buckley D., Greiner J., Heyden K. v. d., Neizvestny S., Potter S., Schwarz R., 2002b, *A&A*, **396**, 895
- Schwöpe A. D., Scipione V., Traulsen I., Schwarz R., Granzer T., Pires A. M., Thorstensen J. R., 2014, *A&A*, **561**, A121
- Sekiguchi K., 1992, *Nature*, **358**, 563
- Shafter A. W., Szkody P., Liebert J., Penning W. R., Bond H. E., Grauer A. D., 1985, *ApJ*, **290**, 707
- Shahbaz T., 2019, in Mignani R., Shearer A., Słowikowska A., Zane S., eds,

- Astrophysics and Space Science Library Vol. 460, Astronomical Polarisation from the Infrared to Gamma Rays. p. 247 ([arXiv:1909.02316](#)), [doi:10.1007/978-3-030-19715-5_10](#)
- Shara M. M., Zurek D., De Marco O., Mizusawa T., Williams R., Livio M., 2012, *AJ*, **143**, 143
- Shen K. J., Quataert E., 2022, *ApJ*, **938**, 31
- Silber A. D., 1992, PhD thesis, Massachusetts Institute of Technology
- Simonsen M., et al., 2014, *AAVSO*, **42**, 177
- Smee S. A., et al., 2013, *AJ*, **146**, 32
- Solheim J. E., 2010, *PASP*, **122**, 1133
- Southworth J., Gänsicke B. T., Marsh T. R., de Martino D., Hakala P., Littlefair S., Rodríguez-Gil P., Szkody P., 2006, *MNRAS*, **373**, 687
- Starrfield S., 1971, *MNRAS*, **155**, 129
- Stockman H. S., Schmidt G. D., Lamb D. Q., 1988, *ApJ*, **332**, 282
- Szkody P., et al., 2002, *AJ*, **123**, 430
- Szkody P., et al., 2003, *AJ*, **126**, 1499
- Szkody P., et al., 2004, *AJ*, **128**, 1882
- Szkody P., et al., 2005, *AJ*, **129**, 2386
- Szkody P., et al., 2006, *AJ*, **131**, 973
- Szkody P., et al., 2007, *AJ*, **134**, 185
- Szkody P., et al., 2009, *AJ*, **137**, 4011
- Szkody P., et al., 2011, *AJ*, **142**, 181
- Thomas H. C., Beuermann K., Burwitz V., Reinsch K., Schwobe A. D., 2000, *A&A*, **353**, 646
- Thorstensen J. R., Skinner J. N., 2012, *AJ*, **144**, 81
- Thorstensen J. R., Fenton W. H., Patterson J., Kemp J., Halpern J., Baraffe I., 2002a, *PASP*, **114**, 1117
- Thorstensen J. R., Fenton W. H., Patterson J. O., Kemp J., Krajci T., Baraffe I., 2002b, *ApJ*, **567**, L49
- Thorstensen J. R., Schwarz R., Schwobe A. D., Staude A., Vogel J., Krumpe M., Kohnert J., Nebot Gómez-Morán A., 2009, *PASP*, **121**, 465
- Thorstensen J. R., Taylor C. J., Peters C. S., Skinner J. N., Southworth J., Gänsicke B. T., 2015, *AJ*, **149**, 128
- Thorstensen J. R., Alper E. H., Weil K. E., 2016, *AJ*, **152**, 226
- Townsley D. M., Bildsten L., 2005, *ApJ*, **628**, 395
- Verbunt F., Zwaan C., 1981, *A&A*, **100**, L7
- Vogel J., Schwobe A. D., Schwarz R., 2011, *A&A*, **530**, A117
- Wang Z., Archibald A. M., Thorstensen J. R., Kaspi V. M., Lorimer D. R., Stairs I., Ransom S. M., 2009, *ApJ*, **703**, 2017
- Warner B., 1995, Cataclysmic variable stars. Cambridge University Press
- Watson C. L., Henden A. A., Price A., 2006, Society for Astronomical Sciences Annual Symposium, **25**, 47
- Watson C., Henden A. A., Price A., 2017, VizieR Online Data Catalog, [p. B/vsx](#)
- Weaver B. A., Blanton M. R., Brinkmann J., Brownstein J. R., Stauffer F., 2015, *PASP*, **127**, 397
- Webb N. A., et al., 2020, *A&A*, **641**, A136
- Webbink R. F., Wickramasinghe D. T., 2002, *MNRAS*, **335**, 1
- Wenger M., et al., 2000, *A&AS*, **143**, 9
- Whyte C. A., Eggleton P. P., 1980, *MNRAS*, **190**, 801
- Wilson D. J., Toloza O., Landstreet J. D., Gänsicke B. T., Drake J. J., Hermes J. J., Koester D., 2021, *MNRAS*, **508**, 561
- Wood J. H., Naylor T., Hassall B. J. M., Ramseyer T. F., 1995, *MNRAS*, **273**, 772
- Woudt P. A., Warner B., Pretorius M. L., Dale D., 2005, in Hameury J. M., Lasota J. P., eds, Astronomical Society of the Pacific Conference Series Vol. 330, The Astrophysics of Cataclysmic Variables and Related Objects. p. 325
- Wu K., 2000, *Space Sci. Rev.*, **93**, 611
- Wyrzykowski L., Hodgkin S., Blogorodnova N., Koposov S., Burgon R., 2012, in 2nd Gaia Follow-up Network for Solar System Objects. p. 21 ([arXiv:1210.5007](#))
- Yanny B., et al., 2009, *AJ*, **137**, 4377
- York D. G., et al., 2000, *AJ*, **120**, 1579
- Šimon V., 2016, *MNRAS*, **463**, 1342

APPENDIX A: NEWLY DISCOVERED CVS

Table A1: New CVs from SDSS III and IV. Distances are from (Bailer-Jones et al. 2021). Apparent magnitudes are from SDSS data release 7 (Abazajian et al. 2009). : Tentative values, * Superhump periods, †Low accretion SU UMa, ‡CVs with unusual state changes, §Period bouncers

SDSS name	Gaia EDR3 source_id	Period (d)	SDSS g (mag)	Distance (pc)	Variable type
J000014.74+255603.1			22.17		CV:
J001231.54+280011.1	2859847683924640384		20.98		WZ Sge:
J002910.96+324125.8			22.12		DN
J004849.86+332832.9	361363704879572736		20.61	763 ⁺³⁵⁸ ₋₂₃₀	SU UMa:
J005421.90+334815.7			22.12		WZ Sge:
J010340.75+200525.9	2788762156951156864	0.158(1):	21.45		IP:
J012212.21+075546.8	2578454444735885056		20.33	343 ⁺¹¹⁹ ₋₇₈	WZ Sge:
J012402.25+211359.7	289388711652054912	0.083475(1)	21.38	688 ⁺³⁵⁷ ₋₂₄₁	Polar
J013421.83+042200.0			21.41		Polar:
J013540.99+340132.9	316371177970255232		22.42		Polar:
J014121.21+062007.6	2562434457240098432		20.77		WZ Sge:
J014732.85+144443.3	2588313902941290112		22.38	907 ⁺⁷²² ₋₃₁₀	Polar
J015253.39-004350.4			20.81		SU UMa:
J015803.40+282303.6	298356019250182016	0.0888104(1)	20.37	254 ⁺²⁰ ₋₁₆	DN
J020712.71-014116.2	2494386992562185088		21.43		Polar:
J023046.26-004531.1			21.68		WZ Sge:
J024215.05-011054.4			22.3		CV:
J072827.34+330741.6			21.94		WZ Sge:
J073605.07+182709.8	672172522242684800		21.83		Polar
J073648.03+200959.7			22.0		CV
J080249.06+363716.4			21.9		WZ Sge:
J080625.73+343244.4		0.0637(1):	21.46		SU UMa:
J081017.41+262238.3			21.31		SU UMa:
J081520.83+335634.1			21.6		WZ Sge:
J082809.87+222004.2	665816516105274496		20.79		CV:
J083404.24+185416.8	662643501643372544		19.23	1634 ⁺⁷²⁶ ₋₄₃₈	Polar
J083549.86+292636.9	704773999783239808		19.88	1244 ⁺⁶⁵⁷ ₋₄₄₂	Polar
J084228.13+462334.4			22.17		CV
J090947.82+110637.0	592059145810439808		20.83	601 ⁺⁶³¹ ₋₂₃₂	WZ Sge:
J091107.84+260617.3			21.53		SU UMa:
J093130.75+335651.2	797435239135183744	0.0799(2):	20.44	797 ⁺⁹⁹⁰ ₋₂₄₈	SU UMa
J101335.56+393826.3	802734507224071936		20.78	882 ⁺⁷⁴¹ ₋₃₁₆	WZ Sge:
J101723.18+375343.4	754291266149306496		21.65		SU UMa
J104245.15+371819.8	751777469035821312		19.7	507 ⁺⁹⁵ ₋₉₁	Polar
J104521.19+362433.0			21.44		WZ Sge:
J115030.59+404151.8	768134186262349568	5.902(2)	21.9	1273 ⁺⁵⁴⁹ ₋₄₅₁	Polar
J115419.05+575751.1	845441772229861760		20.62	1144 ⁺⁴⁴⁹ ₋₃₅₂	ER UMa
J121015.61+351334.4	4029016667559886080		19.38	356 ⁺⁶⁴ ₋₅₈	WZ Sge:
J122808.73+454516.3	1541836947948009472	0.07829(1):	21.66	1599 ⁺⁷⁷⁸ ₋₆₀₈	Polar
J123717.98+365535.2	1519559914656417920		21.22		WZ Sge:
J125716.08+582501.5	1578799436498250368		20.13	953 ⁺¹⁰⁹ ₋₉₉	CV
J133816.44+371639.8			21.66		WZ Sge:
J140430.98+525811.1			21.93		CV
J140430.98+552558.5	1609460864427043072		21.48	1413 ⁺⁷⁷⁶ ₋₆₃₆	DN
J152603.67+382216.4			21.35		WZ Sge:
J155538.12+380250.5	1373544697473750272	0.104(1)	20.39	486 ⁺⁴⁶ ₋₄₉	Polar
J160712.11+392450.6	1379871940214896640	0.08071(1)	21.57		Polar

SDSS name	Gaia EDR3 source_id	Period (d)	SDSS g (mag)	Distance (pc)	Variable type
J160813.59+301952.2			21.46		WZ Sge:
J161853.16+303845.5	1319026547281204480		20.69	1822^{+1404}_{-922}	WZ Sge:
J163620.62+472442.4	1410251583929439744		20.59	708^{+318}_{-227}	WZ Sge:
J171016.94+403127.5			22.08		WZ Sge:
J211652.28+014144.3	2692060074926640000		20.43	2752^{+2087}_{-1558}	SU UMa:
J212406.75+010029.8	2691114426208274176		20.84		WZ Sge:
J213040.11-001319.1			22.34		WZ Sge:
J220818.52+135330.0			21.33		WZ Sge:
J220935.78-001332.5	2678822818216797056		21.8		WZ Sge:
J221333.38+245059.3			21.94		WZ Sge:
J221900.24+201831.1	1778468682222798080	0.140(1)	19.85	821^{+124}_{-98}	DN
J223212.79+260725.1	1880505014843117696		22.26		Polar
J223352.56+225913.4	1875338547143938944		19.89	1294^{+491}_{-329}	Polar
J223623.52+323913.1			21.02		WZ Sge:
J225613.53+191132.9			22.12		WZ Sge:
J225926.51+223902.4			21.81		WZ Sge:
J230319.85+274736.0			22.43		DN:
J232113.45+251822.3	2841125848466425856		20.96	1189^{+715}_{-482}	WZ Sge:
J232553.47+011527.3			21.39		WZ Sge:
J233705.01+314149.4	2871487075361158400		19.64	2574^{+939}_{-1150}	SU UMa:
J235131.68+270907.7	2854471033409793024		21.9	1089^{+467}_{-451}	DN:
J235603.71+001833.3			21.45		WZ Sge:
J183131.63+420220.2	2111270034246759424		16.9	1490^{+162}_{-155}	AM CVn:

This paper has been typeset from a $\text{\TeX}/\text{\LaTeX}$ file prepared by the author.